93-01546/

FINITE ELEMENT MODELLING OF FRACTURE MECHANICS PARAMETERS OF INDUSTRIAL AND LABORATORY SPECIMENS

THIS WORK WAS SUPPORTED BY
THE FEDERAL PANEL ON ENERGY R&D (PERD)

report

by:

Dr. Wieslaw Beres

Work on this project was conducted under the auspices of the
Department of Energy Mines and Resources

16 pp

DSS File Number : 38SQ.23440-0-9212

DSS Contract Number: 23440-0-9212/01-SQ

CANMET Scientific Authority: Dr. George Roy

Ottawa, August 1991

MICROMEDIA

ABSTRACT

In this study, a nonlinear finite element method that predicts the elasto-plastic fracture mechanics parameters (E-PFM) is used. Three parameters were considered: the crack-tip opening displacement (CTOD), the crack-mouth opening displacement (CMOD), and the load point displacement (LPD). The report is divided into two parts. In the first, the E-PFM parameters of a specimen subjected to three-point-bending were investigated. In the second, the critical engineering assesment of a flawed pressure vessel was performed. In both parts of the work numerical modelling was performed using a two-dimensional finite element method program with nonlinear capabilities in plane-strain and plane-stress. Large strains and large deformations were modelled by the updated Lagrangian procedure. All applied plane strain and plane stress finite elements were isoparametric eight-node quadrilaterals with 2 x 2 integration used in the Gauss quadrature formulae. In the crack tip area the quadrilaterals were collapsed along one side to form near-triangular elements. These near-triangular elements were introduced to model crack tip blunting. The initial shape of the undeformed crack tip was modelled, as a circular arc of a 0.005 mm radius. The results represent the first step in verifying the use of the finite element method to predict applied CTOD values as well as the CMOD in more complex structures. The achieved results establish the guidelines for further calculations of the elastic-plastic fracture mechanics parameters of different specimens with varying shapes, crack lengths, and material models.

RÉSUMÉ

Dans cette étude, on a utilisé la méthode des éléments finis nonlinéaires pour résoudre quelques problèmes de la mécanique de la rupture élasto-plastique, EPFM. On a considéré trois paramètres de la théorie: le déplacement de la pointe de la fissure, CTOD, le déplacement maximum des lèvres de la fissure, CMOD, et le déplacement de la pointe de charge.

Le rapport est divise en deux parties. Dans la première partie, on a étudié les paramètres d'analyse EPFM d'une éprouvette fissurée qui était soumise a la flexion trois-point. Dans la seconde partie, on a effectue une analyse d'endommagement d'un tube fissuré sollicité par une pression intérieure.

On a effectué la modélisation numérique par la méthode des éléments finis nonlinéaires dans les milieux plans en déformation planes et contraintes planes. On a modélisé les déplacements et les déformations larges par le processus des étapes successives de Lagrange. Pour modéliser des contraintes planes et des déformations planes, le maillage est construit par les éléments finis isoparamétriques à huit nœds avec la formule d'integration de Gauss 2 x 2.
Dans la région de la fissure, les éléments sont fléchis. La fissure originale est modélisée par un arc de rayon 0.005 mm.

Les résultats font les étapes premières qui seront utilisées dans les études suivantes pour résoudre les problèmes de la mécanique de la rupture élasto-plastique dans des matériaux différentes avec des fissures dont les formes et longueurs varient.

TABLE OF CONTENTS

ABSTRACTS ii

TABLE OF CONTENTS iv

TABLE OF FIGURES vi

1. INTRODUCTION 1

Part I Three-Point-Bend Specimen

2. MATERIALS AND METHODS 4

2.1 Materials 4

2.2 Methods 5

3. FINITE ELEMENT MODELS 6

3.1 Geometry 6

3.2 Boundary conditions 7

3.3 Applied force 8

3.4 Material 9

4. NUMERICAL PROCEDURE 10

5. NUMERICAL RESULTS 12

5.1 Plane strain conditions 12

5.2 Plane stress conditions 13

6. COMPARISON WITH EXPERIMENTAL RESULTS 15

7. CONCLUSIONS 18

Part II Engineering Critical Assessment of a Flawed Pressure Vessel

8. MATERIALS AND METHODS 20

8.1 Materials 20

8.2 Methods 21

9. FINITE ELEMENT MODEL 22

9.1 Geometry 22

9.2 Boundary conditions 23

9.3 Applied force model 24

9.4 Material model 25

10. NUMERICAL PROCEDURE 26

11. NUMERICAL RESULTS 27

12. CONCLUSIONS 29

REFERENCES 30

FIGURES 31

TABLE OF FIGURES

FIGURE 1. Specimen subjected to three-point-bending.

FIGURE 2. Finite element model mesh of the laboratory specimen under the conditions of three-point-bending.

FIGURE 3. Finite element mesh of the laboratory specimen under the conditions of three-point-bending in the vicinity of the crack zone.

FIGURE 4. Finite element mesh at the crack tip.

FIGURE 5. Model of the near-collapsed eight node of quadrilateral element.

FIGURE 6. Details of the initial model of the crack tip.

FIGURE 7. Stress-strain curve of the material model.

FIGURE 8. Details of the material model in the region of small strains.

FIGURE 9. Deformed mesh at the end of the run; plane strain conditions.

FIGURE 10. Deformed mesh in the crack region at the end of the run, plane strain conditions.

FIGURE 11. Crack tip opening displacement; plane strain conditions.

FIGURE 12. Load versus load point displacement (LPD); plane strain conditions.

FIGURE 13. Load versus crack mouth opening displacement (CMOD); plane strain conditions.

FIGURE 14. Stress distribution under the conditions of plane strain in the specimen.

FIGURE 15. Deformed mesh at the end of the run; plane stress conditions.

FIGURE 16. Deformed mesh at the end of the run, crack region; plane stress conditions.

FIGURE 17. Crack tip opening displacement; plane stress conditions.

FIGURE 18. Load versus load point displacement (LPD); plane stress conditions.

FIGURE 19. Load versus crack mouth opening displacement (CMOD); plane stress conditions.

FIGURE 20. Stress distribution under the conditions of plane stress.

FIGURE 21. Comparison of numerical and experimental results for the three-point-bend specimen.

FIGURE 22. Diagram of the pressure vessel.

FIGURE 23. Location of the finite element mesh on the circular ring of a pressure vessel.

FIGURE 24. Finite element mesh model of a cracked segment of the pressure vessel wall.

FIGURE 25. Finite element mesh near the crack zone.

FIGURE 26. Finite element mesh in the crack tip.

FIGURE 27. Results of experimental testing of the weld material of the pressure vessel. Experiments were carried out in CANMET/MTL.

FIGURE 28. Stress-strain curve for the weld material.

FIGURE 29. Stress-strain curve for the weld material model in the zone of small strains.

FIGURE 30. Pressure load applied to the cracked pressure-vessel finite element model at each calculation step.

FIGURE 31. Stress distribution under the conditions of plane strain in the ligament.

FIGURE 32. Undeformed and deformed mesh for the pressure load of 14.96 MPa.

FIGURE 33. Crack tip opening displacement; pressure load of 5.7 MPa.

FIGURE 34. Crack tip opening displacement; pressure load of 9.5 MPa.

FIGURE 35. Crack tip opening displacement; pressure load of 11.4 MPa.

FIGURE 36. Crack tip opening displacement; pressure load of 13.3 MPa.

FIGURE 37. Crack tip opening displacement; pressure load of 13.375 MPa.

FIGURE 38. Crack tip opening displacement; pressure load of 14.725 MPa.

FIGURE 39. The effect of the pressure load on the crack tip opening displacement.

FIGURE 40. The effect of the pressure load on the crack mouth opening displacement.

1. INTRODUCTION

The practical use of elastic-plastic fracture mechanics (E-PFM) requires the analytical evaluation of fracture parameters in the flawed structural components. These parameters are then compared to the fracture toughness of the material which is measured using a standardized test method. The analytical method of predicting the E-PFM parameter must be equally applicable to the test specimen geometry and to the complex geometry of flawed structural components.

In this study, a nonlinear finite element method that predicts the elasto-plastic fracture mechanics (E-PFM) is developed. Three Elastic-Plastic Fracture Mechanics Parameters were considered: the crack-tip opening displacement (CTOD), the crack-mouth opening displacement (CMOD), and the load point displacement (LPD).

An application of the nonlinear finite element method and the associated numerical procedure to calculate the CTOD, CMOD and LPD are the main focus of this study. Analytical CTOD values were determined from the finite element nodal displacements using the 90° intercept procedure.

The report is divided into two parts. In the first part the E-PFM parameters for the three-point-bend specimen are investigated. In the second part of the study, the critical engineering assessment of a flawed pressure vessel was performed.

In both parts of the work numerical modelling was performed using a two-dimensional plane-strain and plane-stress finite element method with nonlinear capabilities. Large strains and large deformations were accounted for by the updated Lagrangian procedure. All applied plane

strain and plane stress finite elements were isoparametric eight-noded quadrilaterals, with 2 x 2 integration order, that was used in the Gauss quadrature formula. In the crack tip area the quadrilaterals were collapsed along one side to form near-triangular elements. These near-triangular elements were introduced to model crack tip blunting. The initial shape of the undeformed crack tip was modelled as a circular arc of radius 0.005 mm .

The results represent the first step in verifying the use of the finite element method to predict applied CTOD values in more complex structures. Also the values for the CMOD were calculated and compared to the experimental values,

The results establish the guidelines for further calculations of the elastic-plastic fracture mechanics parameters of different specimens with varying shapes, crack lengths and material models.

Part I

Three-Point-Bend Specimen

2. MATERIALS AND METHODS

2.1 Materials

A variety of fatigue cracked test specimens can be used to determine the plain strain fracture toughness (K_{Ic}) of metallic materials, such as three-point-bend, compact tension, arc-shaped or disk-shaped compact specimens. The three-point-bend specimen and the compact tension specimen are the most frequently used ones.

The three-point-bend specimen was selected for the study, to compare the results with experimental tests. The dimensions and a material stress-strain characteristics of the specimen represent the laboratory specimen tested obtained from experiments at the laboratories of CANMET/MTL, Energy, Mines, and Resources.

The specimen subjected to three-point-bending is presented in Figure 1. Its dimensions conform to the ASTM Standard, Designation: E813-81. The ratios of the thickness, the width, and the span of the specimen, are 1 : 2 : 8.

The absolute dimensions of the specimen are:

Thickness	B = 10 mm
Width	W = 20 mm
Span	S = 80 mm
Crack length	a = 11.66 mm
Ligament length	b = 8.43 mm .

The specimens is made of the structural steel with the following material parameters:

a) Elastic range of deformation:

Young modulus	E=205 GPa,
Poisson's ratio	ν=0.3;

b) Plastic range of deformation:

Yield strength	σ_y = 430 MPa,
Tangential modulus	T_{mod} = 1140 MPa.

2.2 Methods

The numerical methods used for the fracture mechanics calculation must be able to cover the following factors:

- Singularities in strain and stress.
- Crack tip blunting.
- Large strain in the region of crack tip.

Numerical modelling was performed using a two-dimensional plane-strain and plane-stress finite element method with nonlinear capabilities. Large strains and large deformations were accounted for by the updated Lagrangian procedure.

3. FINITE ELEMENT MODELS

3.1 Geometry

A finite element two-dimensional (2-D) model of the laboratory specimen was prepared. As described in the previous section, the specimen consisted of a standard fracture mechanics specimen subjected to three-point-bending. The FEM elastic-plastic calculations were performed of a three-point-bend specimen under the conditions of plane-strain and plane-stress. The finite element mesh of the model as shown in Figure 2. Since the specimen is symmetric, only one half of the specimen was taken into account during calculations. Proper boundary conditions modelled the effect of the second half of the specimen. All applied plane strain and plane stress finite elements are isoparametric eight-node quadrilaterals, with 2 x 2 integration order used in the Gauss quadrature formula. In the crack tip area the quadrilaterals are collapsed along one side to form near-triangular elements. These near-triangular elements were introduced to model crack tip blunting. Crack tip blunting is possible, if it is modelled by several nodes with independent displacements. Therefore, the initial shape of the undeformed crack tip was modelled, as a circular arc of small radius. The radius of 0.005 mm was used, to represent the value measured in the laboratory specimen.

The model consists of three regions. One region near the zone of supports, and two zones near the crack. The first region consists of twenty rectangular eight-node isoparametric 2-D elements, as presented in Figure 2. The second zone, in the region of plastic deformations, contains fifty curvilinear eight-node elements arranged in five concentrated layers around the

crack tip, as pictured in Figure 3. The third zone, that models the crack tip, consists of ten eight-node quadrilateral elements, initially degenerated into near triangle elements, as presented in Figure 4. For nonlinear analysis, the midnodes on the sides of the quadrilateral element remain in the midpoints but the crack tip nodes are initially placed very close to each other, as shown in Figure 5. During a step by step solution of the finite element model, these nodes are allowed to displace, forming the crack tip opening. To model the initial shape of the undeformed crack tip, the degenerated nodes were arrange to form a circular arc of the 0.005 mm radius, as pictured in Figure 6. The entire finite element mesh consists of 284 nodes and 80 elements. After the boundary conditions were applied , the discussed finite element model consisted of 552 equations, with a maximum half bandwidth equal of 110.

3.2 Boundary conditions

The application of proper boundary conditions allows to model only one half of the specimen, as well as to model the existence of the crack in the structure. The following boundary conditions were applied (Figure 2):

(i) The nodes on the lines 1-32 and 32-31 are free to move along the Z-axis, but are fixed along the Y-axis;

(ii) The node number 8 is free to move along the Y-axis, but it is fixed along the Z axis. Thus, modelling the roller support is possible;

(iii) All displacements along the X-axis are fixed;

(iv) All node rotations are fixed.

This boundary conditions allow to model of the loading point deflection by imposing the Z-axis displacement at the finite element node 1.

3.3 Applied force

Two methods of exerting an external action on the structure were taken into account: force control, and displacement control. The displacement control method was chosen for the calculation. This method, allowed for the application of fewer number of steps. Also the number of iterations to achieve the convergence was fewer with this method.

External displacement increments were applied at the finite element node 1 (Figure 2) in the negative vertical direction of the Z-axis. As it was already mentioned, the rolling support was applied at the finite element node number 8, see Figure 1. This arrangement closely models the real laboratory testing conditions of the specimen.

3.4 Material

The material model chosen for the nonlinear analysis must fit closely the material stress-strain curve obtained from the laboratory experiments. The multilinear elastic-plastic material model, with the von Mises yield criterion, was used in the calculations. Figures 7 and 8 present this material model, that was adopted on the basis of the results of static material tests, carried out in the Energy, Mines and Resources CANMET/MTL Laboratory. It can be seen that, for calculation purposes, the material model was extended beyond the experimentally measured stress and strain region. The initial value of plastic strain is zero. The linear isotropic strain hardening model was incorporated in the discussed material model. In the linear strain range the following material parameters were applied:

Young modulus	E=205 GPa,
Poisson's ratio	ν=0.3 .

4. NUMERICAL PROCEDURE

Two-dimensional (2-D) plane-strain and plane-stress finite element method with nonlinear capabilities was used for the calculations. Large strains and large deformations were accounted for by the updated Lagrangian formulation.

For each calculation, external displacement increments were applied at the finite element node 1 (Figure 2) in the negative vertical direction of the Z-axis. Ten equal increments were used, each displacement increment of 0.4 mm. Therefore, total displacement δ of 4 mm was applied.

At each step an equilibrium iteration was performed. In the iteration process the balance of deformation forces and externally applied forces is found. The full Newton method of iteration with line search procedure was applied. Energy convergence criteria were used to establish the equilibrium. Also, at each step of the calculations the stiffness matrix was updated.

The calculations were repeated for the plane strain and plane stress conditions.

In the course of each run, the appropriate specimen load was found from the Z-axis reaction in the node 8 (Figure 2). Due to the symmetry of the modelled specimen, this reaction was multiplied by 2, to get the force that is applied to the finite element model.

The final results, i.e. the specimen load and the loading point displacement were normalized using the following formulas:

$$Normalized\ displacement = \frac{\delta}{W}$$

$$Normalized\ force = \frac{4FW}{Bb^2\sigma_y}$$

where

δ is the load point displacement (LPD),

W is the width of the specimen,

F is the applied force,

B is the specimen thickness,

b is the length of a ligament,

σ_y is the yield stress of the specimen material.

This normalization yields the dimensionless quantities that allow for the future comparison of the results obtained by application of different methods of calculation.

5. NUMERICAL RESULTS

5.1 Plane strain conditions

Figures 9, 10 and 11 present the deformed shape of the specimen in the plane strain condition at the end of the run , i.e. for the LPD δ equal 4 mm. Figure 9 shows the entire deformed mesh, Figure 10 illustrates the crack tip region, whereas the Figure 11 presents the details of the crack tip opening displacement (CTOD). The E-PFM parameters, that is crack tip opening displacement and the crack mouth opening displacement (CMOD) are found from the presented deformed shapes. The details of the calculation of CMOD are given in the Figure 10, whereas the illustration of the CTOD definition is shown in Figure 11. The 90°-intercept procedure was applied.

Figures 12 and 13 present the load versus load point displacement (LPD) and load versus CMOD curves, respectively, obtained for the entire range of applied displacement δ from zero to the full range of 4 mm. At both curves, the two regions - linear and nonlinear ones are clearly distinguished.

At the step 9 of the run, for the plane strain condition, the following E-PFM parameter values were obtained:

$$\delta_9 = 3.2 \text{ mm},$$

$$F_9 = 8222 \text{ N},$$

$$CMOD_9 = 2.418 \text{ mm},$$

$$CTOD_9 = 0.850 \text{ mm}.$$

These values are next compared to the values obtained from the laboratory experiments.

In Figure 14, the stress distribution for the entire specimen in plane strain conditions is shown. The stress line contours depict the effective stress, i.e. the equivalent stress calculated from the maximum distortion energy theory, called a Huber-von Mises-Hencky formula

$$\sigma_{eq} = \sqrt{\sigma_y^2 + \sigma_x^2 - \sigma_y \sigma_x + 3\tau_{yx}^2}$$

The isolines are drawn for stresses from 100 MPa to 600 MPa, with a step of 100 MPa. Some discontinuities of the stress isolines in the area remote from the crack tip are inherent in the finite element method, due to a relatively large size of the finite elements in this area.

The figure presents the distribution of the high stress area around the crack tip. It can be seen that this area forms the strip, that starts from the crack tip, and goes through the entire ligament. The effective stress in this area is above 500 MPa, that is the entire ligament of the specimen has plasticized. Therefore, the complete collapse in the ligament region was reached when the effective stress exceeded the nominal value, which occurred in the calculation step 9, that corresponds to the unit normalized force value of 8222 N.

5.2 Plane stress conditions

Figures 15, 16 and 17 present the deformed shape of the specimen in the plane stress condition at the end of the run , i.e. for the LPD δ equal to 4 mm. Figure 15 shows the entire deformed mesh, Figure 16 illustrates the crack tip region, whereas the Figure 17 presents the

details of the crack tip opening displacement. The E-PFM parameters crack tip opening displacement and the crack mouth opening displacement was found from the presented deformed shapes. The 90° intercept procedure was applied for calculation of CMOD, as shown in Figure 17.

Figures 18 and 19 present the load versus Load Point Displacement and load versus CMOD curves, respectively, obtained for the entire range of applied displacement δ from zero to the full range of 4 mm. At both curves, the two regions, linear and nonlinear, are clearly distinguished.

At the step 9 of the run, for the plane stress condition, the following E-PFM parameter values were obtained:

$$\delta_9 = 3.2 \text{ mm},$$

$$F_9 = 6068 \text{ N},$$

$$CMOD_9 = 2.460 \text{ mm},$$

$$CTOD_9 = 0.855 \text{ mm}.$$

These values, together with the corresponding values for plane strain conditions, are next compared to the values obtained from the laboratory experiments.

In Figure 20, the stress distribution for the entire specimen in plane stress conditions is shown. The shaded isobands depict the effective stress, i.e. the equivalent stress calculated from the maximum distortion energy theory, see page 13.

The solid colored areas are drawn for stresses from 100 MPa to 600 MPa, with a step of 100 MPa. Some discontinuities of the stress isoband in the area remote to the crack tip are inherent in the finite element method, due to a relatively large size of the finite elements in this area.

The figure presents the distribution of the high stress area in the finite element model. There are two high stress area in the ligament of the specimen - one in the vicinity of the crack tip, and the second in the zone of the load point. The stresses in this zones are higher than 600 MPa. In the middle of the ligament in the main symmetry plane of the specimen the stresses are in the range of 400-500 MPa. When compared to the yield point of the material model used for calculation, these figures show that the entire ligament of the specimen has plasticized. Therefore, the complete collapse in the ligament region was reached when the effective stress exceeded the nominal value, which occurred in the calculation step 9, that corresponds to the unit normalized force value of 6068 N.

6. COMPARISON WITH EXPERIMENTAL RESULTS

The results obtained for the plane strain and plane stress conditions were compared to the experimental records obtained from tests performed on three-point-bend specimens in the INSTRON setup at MTL. Table 1 and Figure 21 present the results of the comparison.

Table 1. Comparison of numerical and experimental results, for the three-point-bend specimen.

Parameters	Numerical		Experimental
	Plane strain Conditions	Plane stress Conditions	B = 10 mm
δ, mm	3.2	3.2	3.11
F, N	8222	6068	6300
CMOD, mm	2.418	2.460	2.62
CTOD, mm	0.850	0.855	-

- = No data available

Figure 21 presents the experimental results, obtained in the INSTRON setup at MTL, together with the numerical results for the plane strain and plane stress conditions. The load versus load point displacement diagrams are drawn as the experimental results. The experiments were carried out for various thicknesses of specimen that vary in the range of 10-50 mm, and for two ambient temperatures: +25 and -80 °C. Both, the load and the displacement were normalized according to the formulas given on the page 11.

It could be seen from the figure that the normalized experimental results obtained for the specimens of various thicknesses, at different temperatures for the plastic range of applied displacement fit closely the normalized numerical curves obtained for the plane strain conditions.

This agreement is not so obvious for the elastic range. The numerical results for the plane strain condition fit the experimental results much closer than that for the plane stress condition. The reason for that is that too few calculation steps were chosen for the transition zone between elastic and plastic range.

Summarizing, the numerical results indicate good compatibility of the numerical predictions with the experimental records obtained from tests performed on three-point-bend specimens in the INSTRON setup at MTL.

7. CONCLUSIONS

1. The numerical results obtained for the model of three-point-bending indicate good compatibility of the numerical predictions with the experimental records obtained from tests performed on three-point-bend specimens in the INSTRON setup at MTL. The differences between the actual experimental load and the numerical predictions for the plane strain and plane stress conditions for the load point displacement are 3% and 3% respectively, whereas, the predicted loads for the two states bound the experimental records, as documented elsewhere and consistent with the theory (Keim and Muller, 1989).

2. The number of nodes and finite elements, the type and integration order of elements, as well as the boundary conditions, the applied force model, the initial shape of the crack tip, and the number of steps applied for calculation, were chosen properly.

3. An important factor for the proper modeling of the crack tip is the creation of the initial crack tip shape for the undeformed mesh. The numerical experiments showed that, for the case of three-point bend specimen discussed in the report, the model with the initial crack tip radius of 0.005 mm generated proper results.

4. The achieved results establish the guidelines for further calculations of different fracture specimens with varying shapes, crack lengths and material models.

Part II

Engineering Critical Assessment

of

a Flawed Industrial Pressure Vessel

8. MATERIALS AND METHODS

8.1 Materials

As a part of the Engineering Critical Assessment (ECA) Program, the analysis of a flawed industrial pressure vessel was performed by several researchers, e.g. (Jutla and Chakravarti, 1990) or (Oddy and McDill, 1990), and the results of these calculations and numerical analyses are compared with those obtained from the experimental test carried out on a real size vessel.

In this part of the report, the numerical analysis of the critical internal pressure was numerically performed. Also the CTOD and CMOD values for the range of internal pressures in the vessel were found. The critical internal pressure was defined as a plastic collapse of a vessel wall.

The Figure 22 shows the pressure vessel analyzed. The main geometrical parameters of the vessel are

Internal diameter	1800 mm
External diameter	1857.2 mm
Wall thickness	28.6 mm
High	5800 mm
Material	ASME SA 516 Grade 70 steel.

The vessel was subjected to a non-destructive test around the welded regions by Hanson Materials Engineering. The results from these tests were presented by Jutla and Chakravarti (1990).

The circumferential weld denoted C3, Figure 22, was selected for analysis. The largest axial flaw in this weld measures 7.62 mm, according to Jutla and Chakravarti (1990). Hence the ligament length is 20.98 mm.

The planar model of the weld consists of a circumferential ring with the external and internal diameters of 1857.2 and 1800 mm, respectively, with the crack model in it. Since the geometry indicates circular symmetry only the ring segment was modeled. This approach considerably decreases the complexity of the task, resulting also in a decrease of time for data preparation and computations.

The weld ring with the segment analyzed is presented in Figure 23.

8.2 Methods

Numerical modelling was performed using a two-dimensional plane-strain finite element method with nonlinear capabilities. Large strains and large deformations were accounted for by the updated Lagrangian procedure.

9. FINITE ELEMENT MODEL

9.1 Geometry

A finite element, two-dimensional (2-D) model of the axial crack in the pressure vessel analyzed was prepared. As described in the previous section, the model consists of a circular segment of the vessel wall with the axial crack in the weld.

The finite element mesh for performing elastic-plastic calculations of a cracked vessel wall in plane-strain condition is shown in Figure 24. Since the obvious circular symmetry of the vessel wall exist, only one half of the segment was taken into account during calculations. Proper boundary conditions modelled the effect of the second half of the segment. All applied plane strain finite elements are isoparametric eight-node quadrilaterals, with 2 x 2 integration order used in the Gauss quadrature formula. In the crack tip area the quadrilaterals are collapsed along one side to form near-triangular elements. These near-triangular elements were introduced to model crack tip blunting. Crack tip blunting is possible, if it is modelled by several nodes with independent displacements. Therefore, the initial shape of the undeformed crack tip was modelled as a circular arc of small radius. The radius of 0.005 mm was used.

The lines 1-3-5-9 and 2-4-6-10 of the model (Figure 24) form the circular segment of 3.5° angle. It consists of two circular arcs of radii 0.9000 m and 0.9286 m. Lines 1-2 and 9-10 are normal to these arcs.

The model consists of three regions. Two zones near the crack tip and one zone adjacent to the crack tip. The first region consists of twenty curvilinear eight-node isoparametric 2-D elements, as presented in Figure 24. The second zone, in the region of plastic deformations,

contains fifty curvilinear eight-node elements arranged in five concentrated layers around the crack tip, as pictured in Figure 25. The third zone, that models the crack tip, consists of ten eight-node quadrilateral elements, initially degenerated into near triangle elements, as presented in Figure 26. For nonlinear analysis, the midnodes on the sides of the quadrilateral element remain in the midpoints but the crack tip nodes are initially placed very close to each other, as shown in Figure 5.

The entire finite element mesh consists of 284 nodes and 80 elements. After applying the boundary conditions, the discussed finite element model consists of 552 equations, with a maximum half bandwidth equal to 110.

9.2 Boundary conditions

The application of proper boundary conditions allows to model only a circular segment of the pressure vessel wall, as well as to model the existence of the crack in this wall. Since only a segment of the 3.5° angular measure belonging to the circular ring was taken into account, the boundary conditions on the side lines of the segment model the remainder of the structure.

To model the boundary conditions on the line 9-10 (Figure 24), the skew coordinate system was used. This screw system (a,b,c) is defined in the terms of the global (X,Y,Z) coordinate system. The **a** vector of the screw system is parallel to the X-axis, the **b** vector is on the Y-Z plane and is inclined at -86.5° to the Z-axis, whereas the **c** vector is calculated so that it is orthogonal to both a-axis and b-axis. An application of the global coordinate system (X,Y,Z) and the skew system (a,b,c) made it possible to apply the following boundary conditions:

(i) The nodes on the lines 1-32 and 32-31 are free to move along the Z-axis, but are fixed along the Y-axis.

(ii) The nodes on the line 9-10 are free to move along the b-axis of the screw coordinate system, but are fixed along the c-axis of this system.

(iii) All displacements along the X-axis are fixed.

(iv) All node rotations are fixed.

These boundary conditions allow also to model the internal pressure in the discussed pressure vessel, by applying the line distributed loads directed in the direction normal to the line 1-3-5-9.

9.3 Applied force model

The internal pressure load was applied to the segment of the pressure vessel wall weld that was analyzed.

The final pressure of value 14.9625 MPa was applied to the lines 1-3, 3-5, and 5-9, Figure 24, in the direction that was normal to these lines. The finite element software recalculates the

applied pressure load into the nodal point external forces for all nodes located on the lines 1-3, 3-5, and 5-9. Both, the values and the direction of applied forces are taken into account.

This load was applied in the incremental steps, as described in the Section 10.

9.4 Material model

The material model chosen for the nonlinear analysis must fit closely the material stress-strain curve obtained from the laboratory experiments. Figure 27 presents the results of tests of a weld material of the pressure vessel analyzed. These tests were carried out in CANMET/MTL Laboratory. On the basis of these tests, the multilinear elastic-plastic material model, with the von Mises yield criterion, was used in the calculations. Figure 28 present this material model. For calculation purposes, the material model was extended beyond the experimentally measured stress and strains region. The linear value of plastic strain is zero. The linear isotropic strain hardening model was used in the discussed material model. In the linear strain range the following material parameters were applied:

Young modulus E=20 GPa,

and Poisson's ratio ν=0.3 .

10. NUMERICAL PROCEDURE

Two-dimensional (2-D) plane-strain finite element method with nonlinear capabilities was used for the calculations. Large strains and large deformations were accounted for by the updated Lagrangian formulation.

The pressure load increments were applied at the finite element nodes that belong to the line 1-3-5-9 (Figure 24), in the direction normal to that line. To get the convergency, the pressure load increment was decreased with increasing number of steps. Figure 30 shows the pressure values applied at each step.

At each step an equilibrium iteration was performed. In the iteration process the balance of deformation forces and externally applied pressure forces was found. The full Newton method of iteration with line search procedure was applied. Energy convergence criteria was used to establish the equilibrium. Also, at each step of calculations the stiffness matrix was updated.

For each calculation step the state of stress in the area of crack tip was analyzed. Failure was assumed to occur, if a plastic collapse condition developed. The plastic collapse was defined as a condition in which all finite elements in the ligament, bounded by the nodes 1, 2, 5, and 6, developed the effective stress that exceeds the yield point of material.

Also, the crack tip opening displacements were found for each calculation step, using the 90°-intercept procedure.

11. NUMERICAL RESULTS

Figure 31 presents the stress distribution in the area surrounding the crack in the wall for the calculation step 25. The stress line contours depict the effective stress, i.e. the equivalent stress calculated from the maximum distortion energy theory, called a Huber-von Mises-Hencky formula, page 13.

The isolines are drawn for stresses from 100 MPa to 600 MPa, with a step of 100 MPa. Some small discontinuities of the stress isolines in the area remote to the crack tip are inherent in the finite element method, due to a relatively large size of the finite elements in this area.

The figure presents the distribution of the high stress area around the crack tip. It can be seen that this area forms the strip, that starts from the crack tip, and goes through the entire ligament. The effective stress in this area is above 500 MPa, that is the entire ligament of the specimen has plasticized. The load pressure applied at this step was the smallest one that caused formation of the plastic zone through the entire ligament. Therefore, the complete collapse in the ligament region was reached when the effective stress exceeded the nominal value, which occurred in the calculation step 24, that corresponds to the pressure load of 14.96 MPa. Therefore, the pressure, equal to 15 MPa was considered as the failure pressure.

Figure 32 presents the deformed shape of the mesh in the plane strain condition for the calculation step 25, i.e. for the load pressure equal to 14.96 MPa. It can be seen that for this critical pressure the vessel diameter considerably increased. The increase in diameter of deformed circular ring was of 82.4 mm, from its initial value of 1800 mm, that is an increase of 4.6 %. The

CTOD and CMOD values for this critical pressure load were equal to 1.667 mm and 3.14 mm, respectively.

It should be noted, that weld material model use for the calculation is characterized by a much smaller value of Young's modulus than that for the steel. This resulted is relatively large values of CTODs and CMODs.

Figures 33-38 show the deformed shape of the crack tip for the subsequent load steps, that is for increased values of applied pressure loads. Small irregularities in the deformed mesh in the crack tip elements are due to a high strain in these elements. To overcome this problem, the model should be remeshed with the crack tip elements decreased. Since these irregularities effected the CTOD values only slightly, the remeshing was not carried out.

Figure 39 presents the effect of the model pressure load on the crack tip opening displacement values. It can be seen that with the increase of the pressure load, the CTOD values increase exponentially.

Figure 40 presents the effect of the model pressure load on the crack mouth opening displacement values. It can be seen that, analogically to the CTOD values, with the increase of the pressure load the CMOD values increase exponentially.

12. CONCLUSIONS

1. The circumferential weld denoted C3 (Figure 22) was taken into account. The largest axial flaw in this weld measures 7.62 mm.

2. The critical pressure in the cracked weld region is 15 MPa. For this pressure value entire ligament around the largest crack has plasticized.

3. The critical value of CMOD, as the only measurable parameter is 3.14 mm, which can be converted into the crack tip opening displacement and compared with the experimentally obtained data.

4. The achieved results establish the guidelines for further calculations of different flawed pressure vessels with weld shapes, crack lengths and material models.

REFERENCES

Bass., B.R., Keeney-Walker, J., et al., 1989, *Application of ADINA to Viscoplastic Dynamic Fracture Mechanics Analysis*. Computers and Structures, Vol. 32, No. 3/4, pp. 815-824.

Jutla, T., Chakravarti, A. 1990, *Fracture Prediction of a Defective Vessel - Preliminary Analysis*. Materials Technology Centre, Fleet Technology Ltd., Ottawa, Report No. E93711C.

Keim, E., Muller, G., 1989, *Nonlinear Analysis of Fracture Mechanics Problems*. Computers and Structures, Vol. 32, No. 3/4, pp. 737-743.

Larsson, L.H., 1983, *A Calculational Round Robin in Elastic-Plastic Fracture Mechanics*. Int. J. of Pressure Vessels and Piping, Vol. 11, pp. 207-228.

Oddy, A.S., McDill, J.M.J., 1990, *Numerical Analysis of a Flawed Pressure Vessel*. CANMET, Metals Technology Laboratories, Report No.MTL 90-45(TR).

Schmitt, W., 1984, *Three Dimensional Finite Element Simulation of Post-Yield Fracture Experiments*. Computational Fracture Mechanics-Nonlinear and 3-D Problems, The 1984 Pressure Vessel and Piping Conference and Exhibition, San Antonio, Texas, ASME, pp. PVP Vol. 85, AMD Vol. 61.

Siegele, D., 1989, *3D-Crack Propagation Using ADINA*. Computers and Structures, Vol. 32, No. 3/4, pp. 639-645.

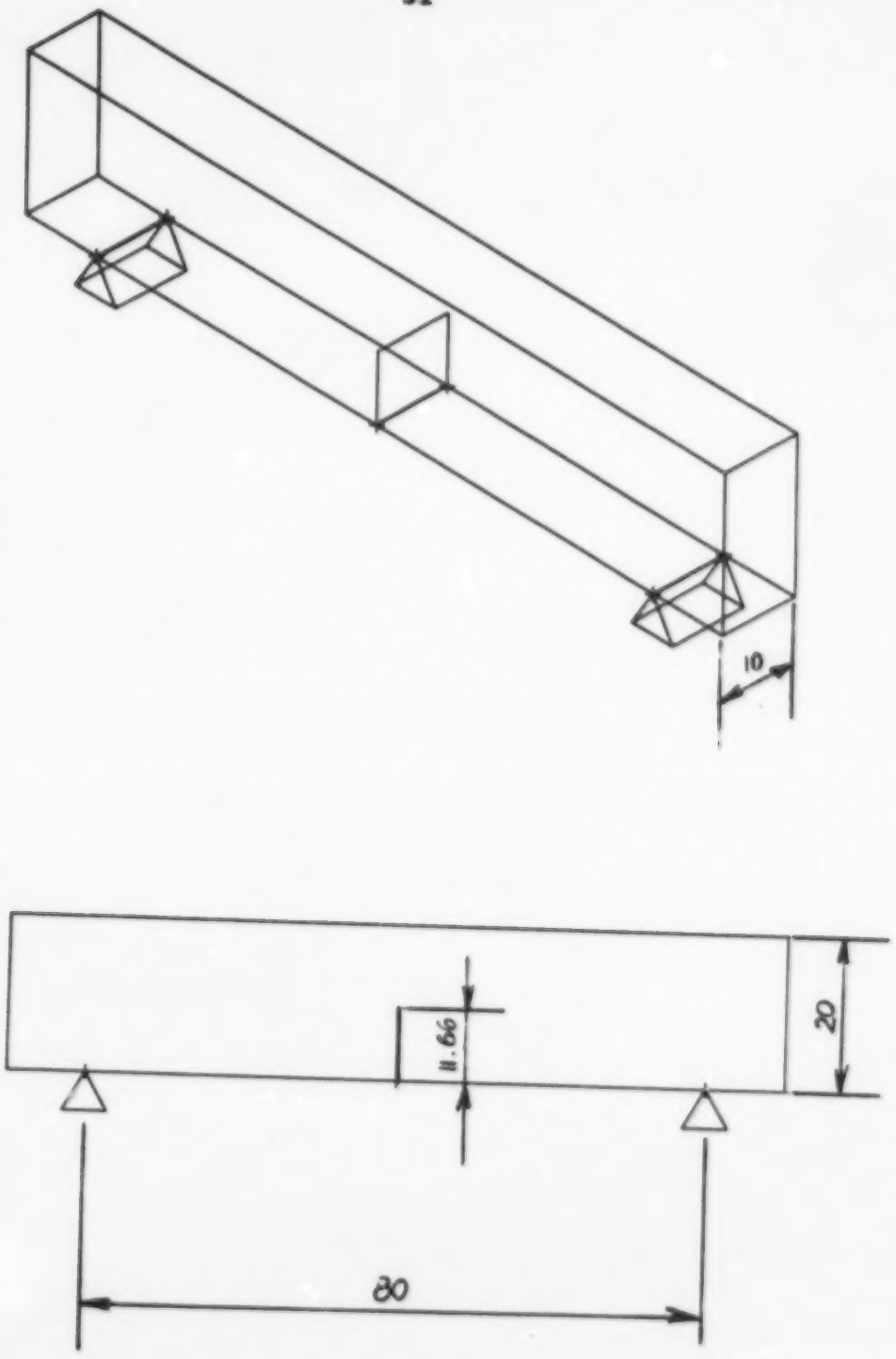

FIGURE 1. Specimen subjected to three-point-bending.

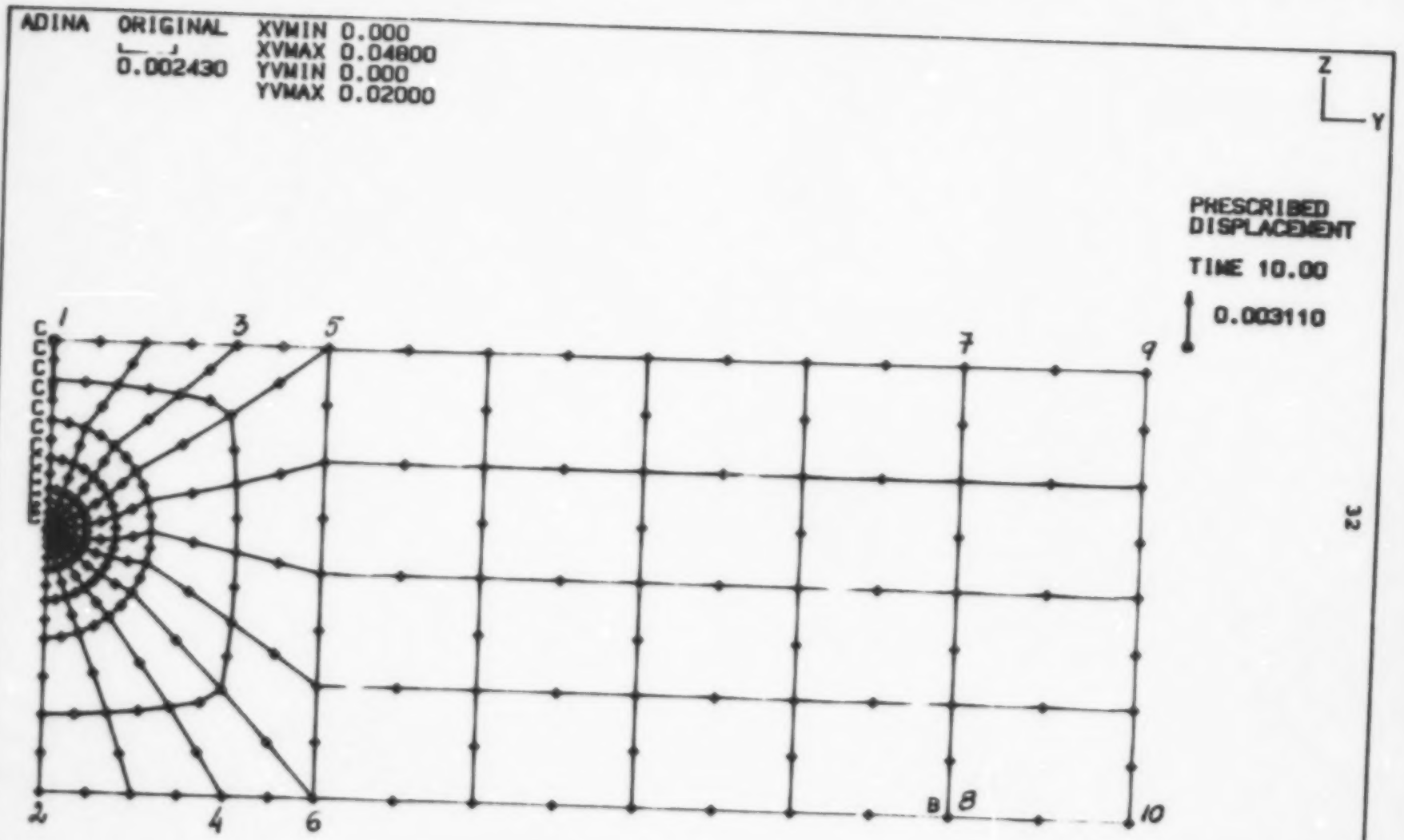

FIGURE 2. Finite element model mesh of the laboratory specimen under the conditions of three-point-bending.

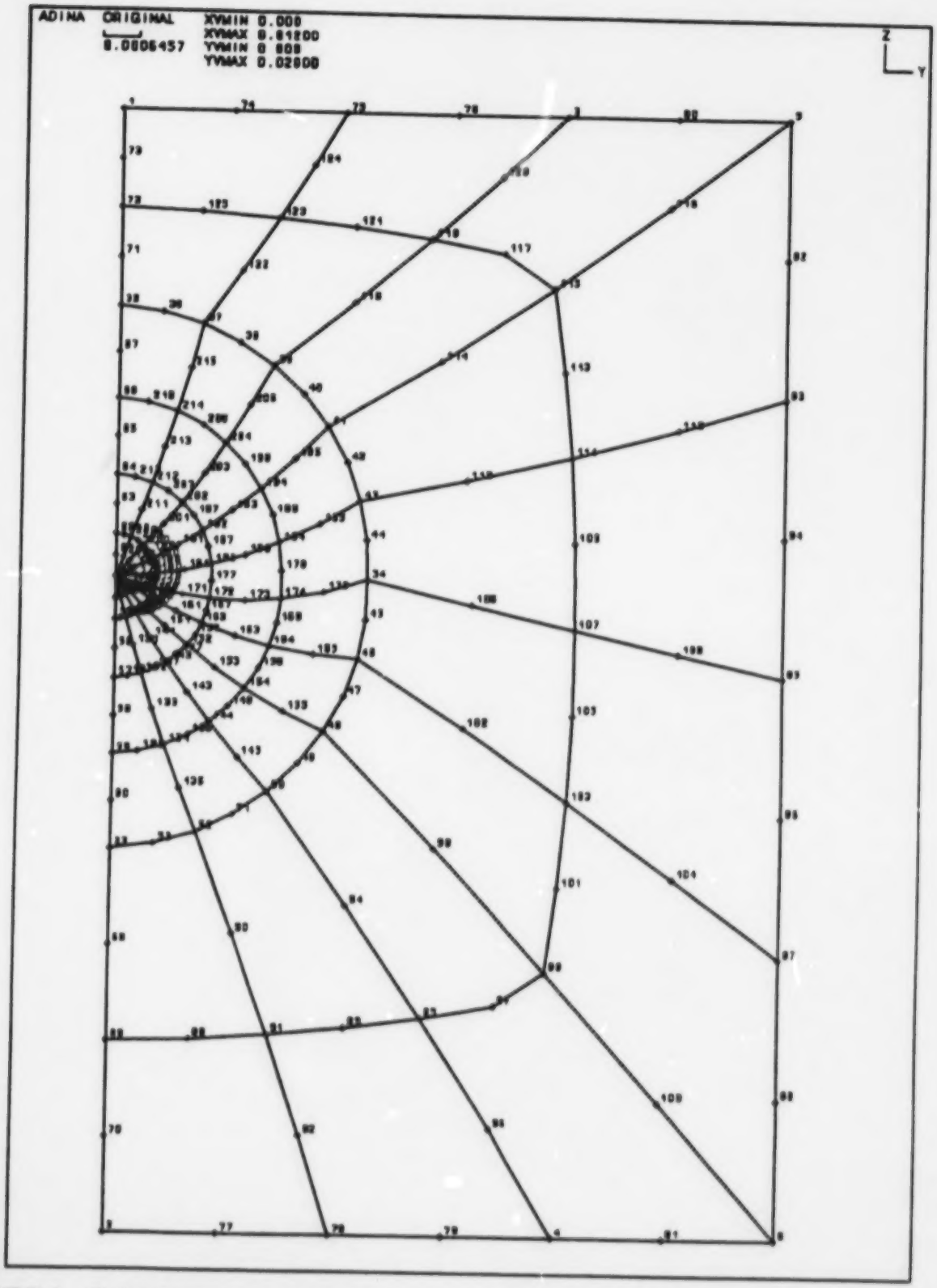

FIGURE 3. Finite element mesh of the laboratory specimen under the conditions of three-point-bending in the vicinity of the crack zone.

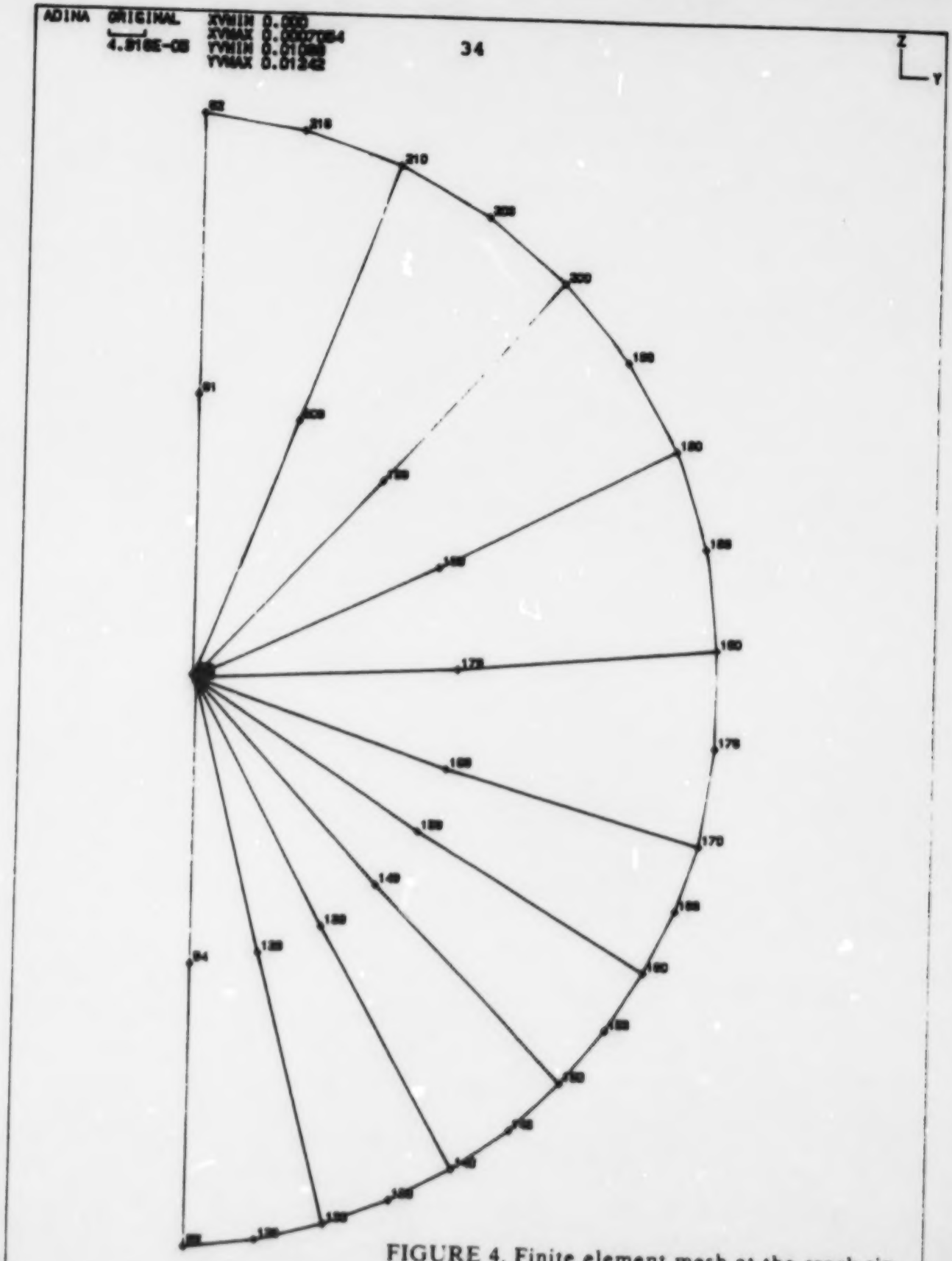

FIGURE 4. Finite element mesh at the crack tip.

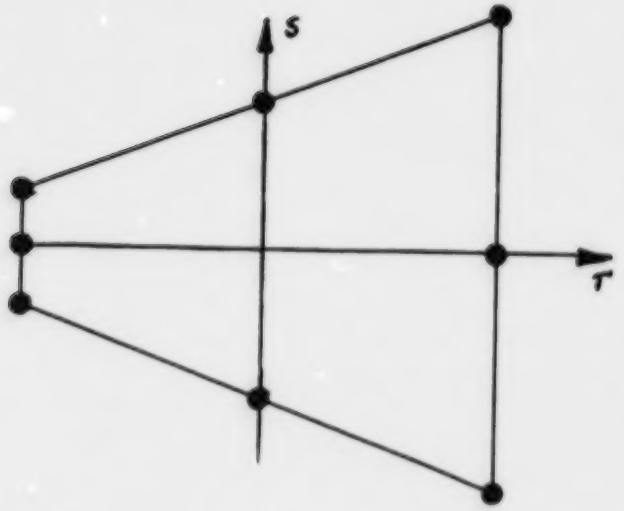

FIGURE 5. Model of the near-collapsed eight node quadrilateral element.

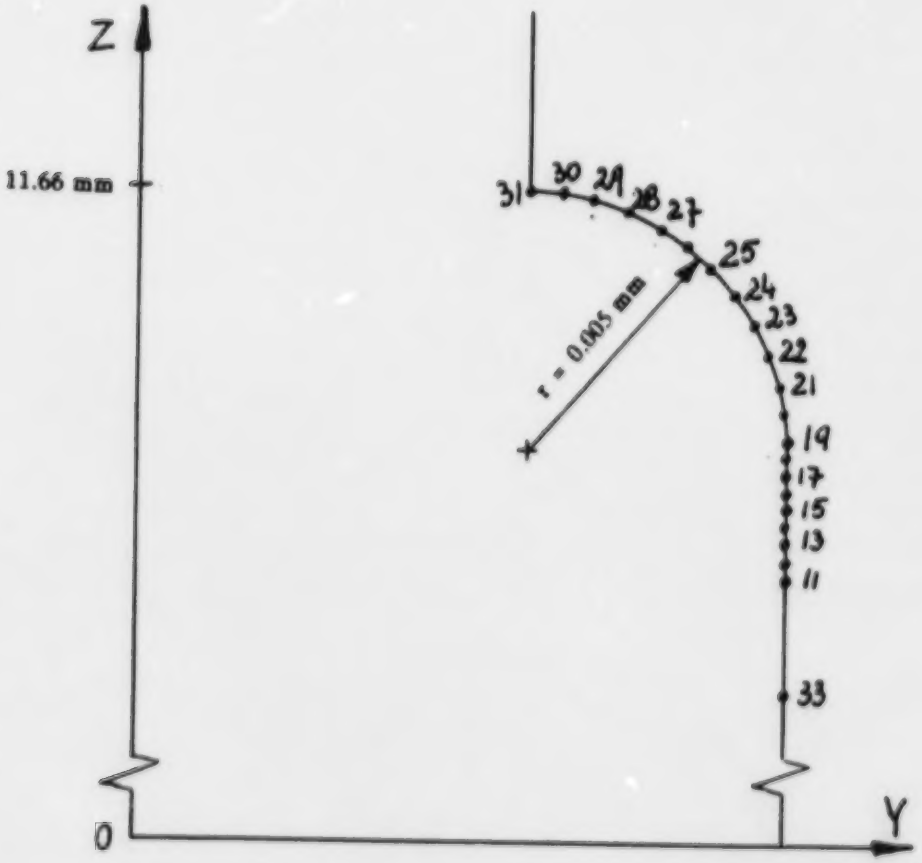

FIGURE 6. Details of the initial model of the crack tip.

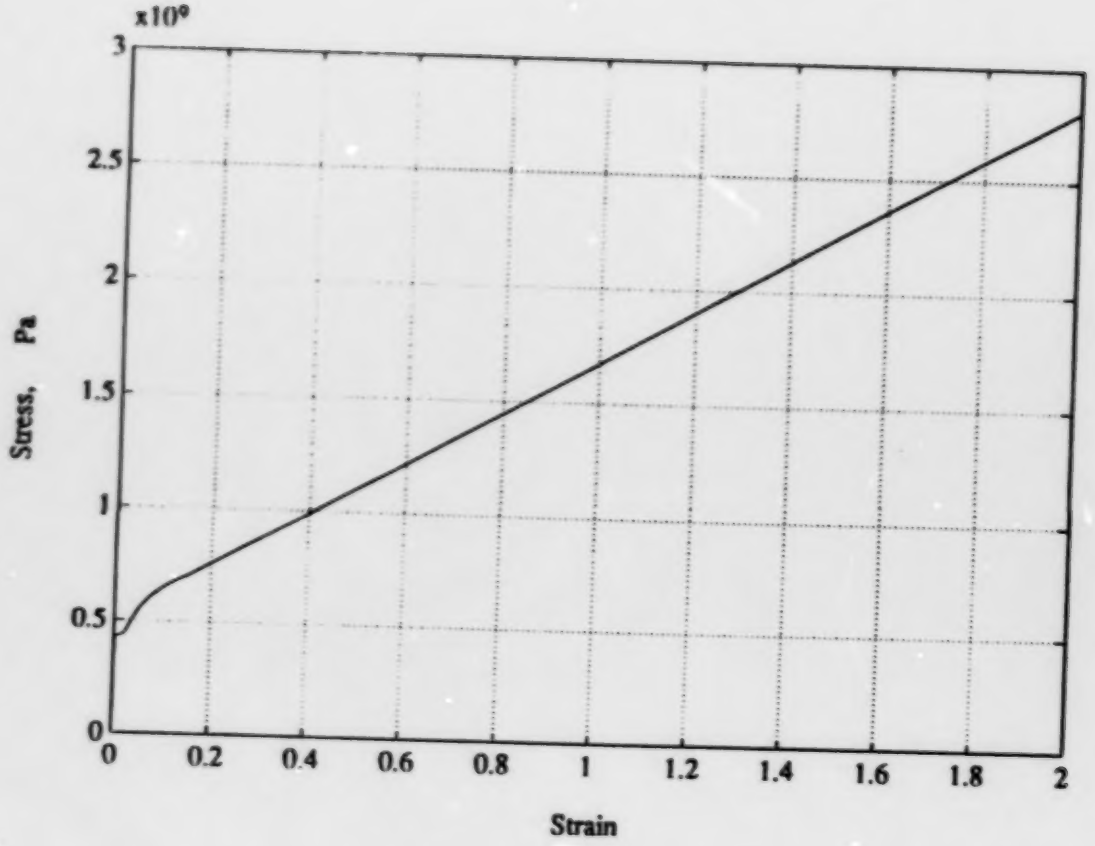

FIGURE 7. Stress-strain curve of the material model.

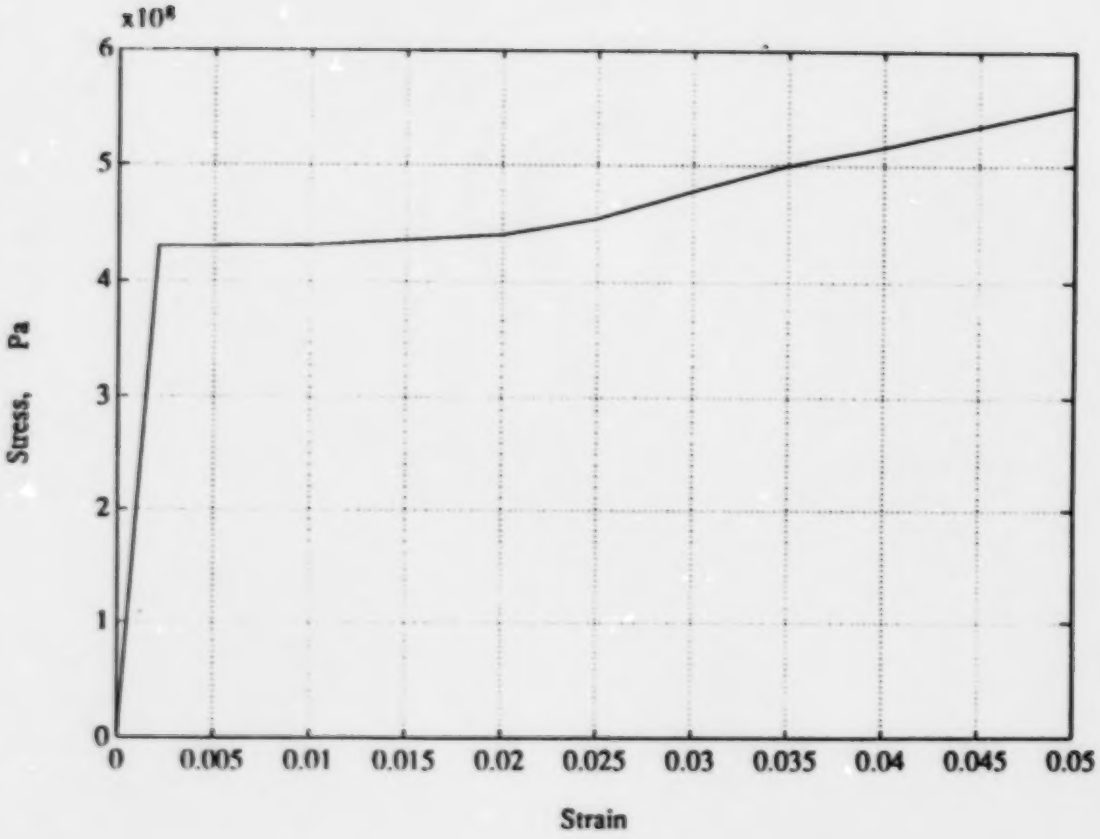

FIGURE 8. Details of the material model in the region of small strains.

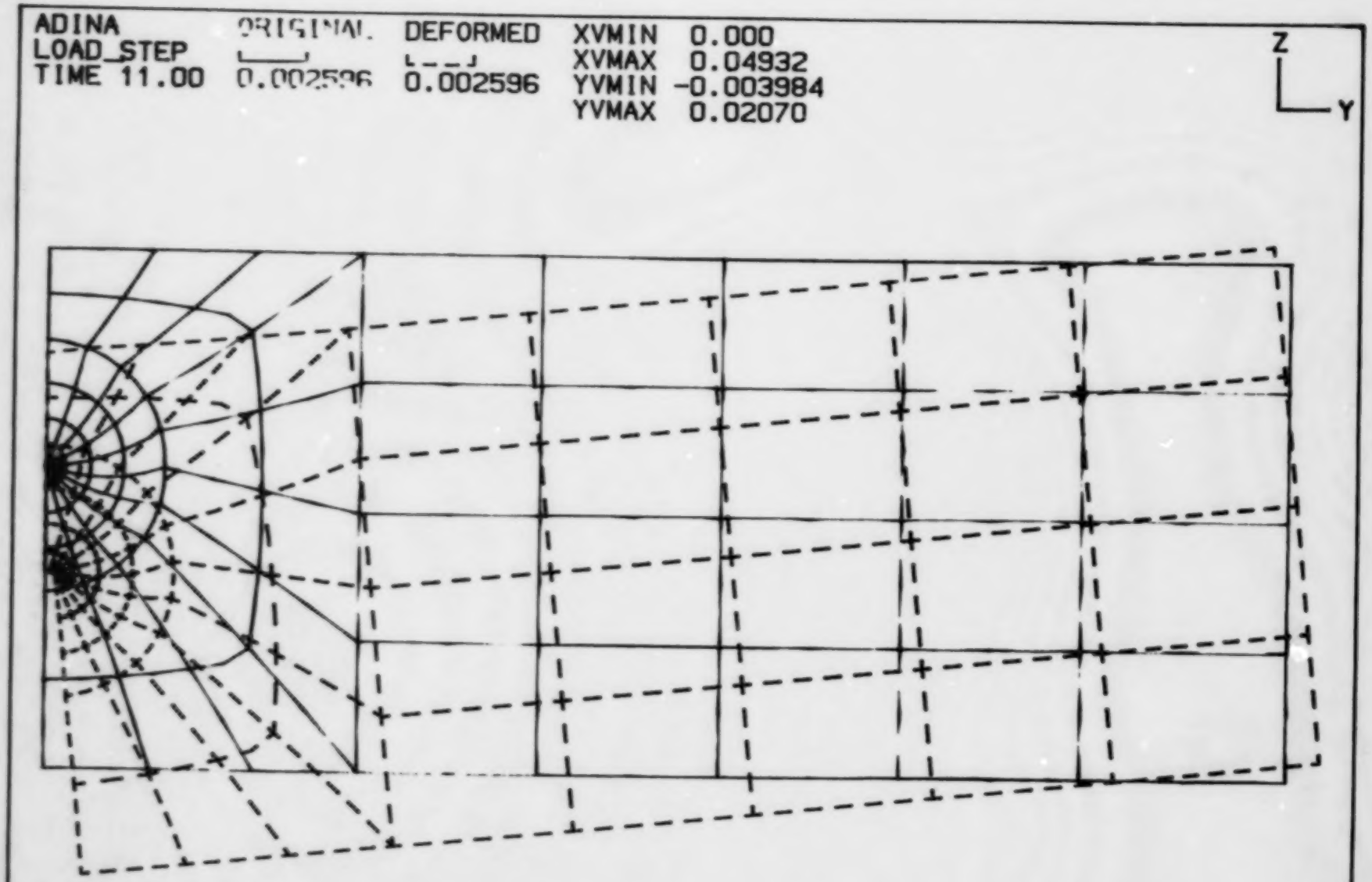

FIGURE 9. Deformed mesh at the end of the run, plane strain conditions.

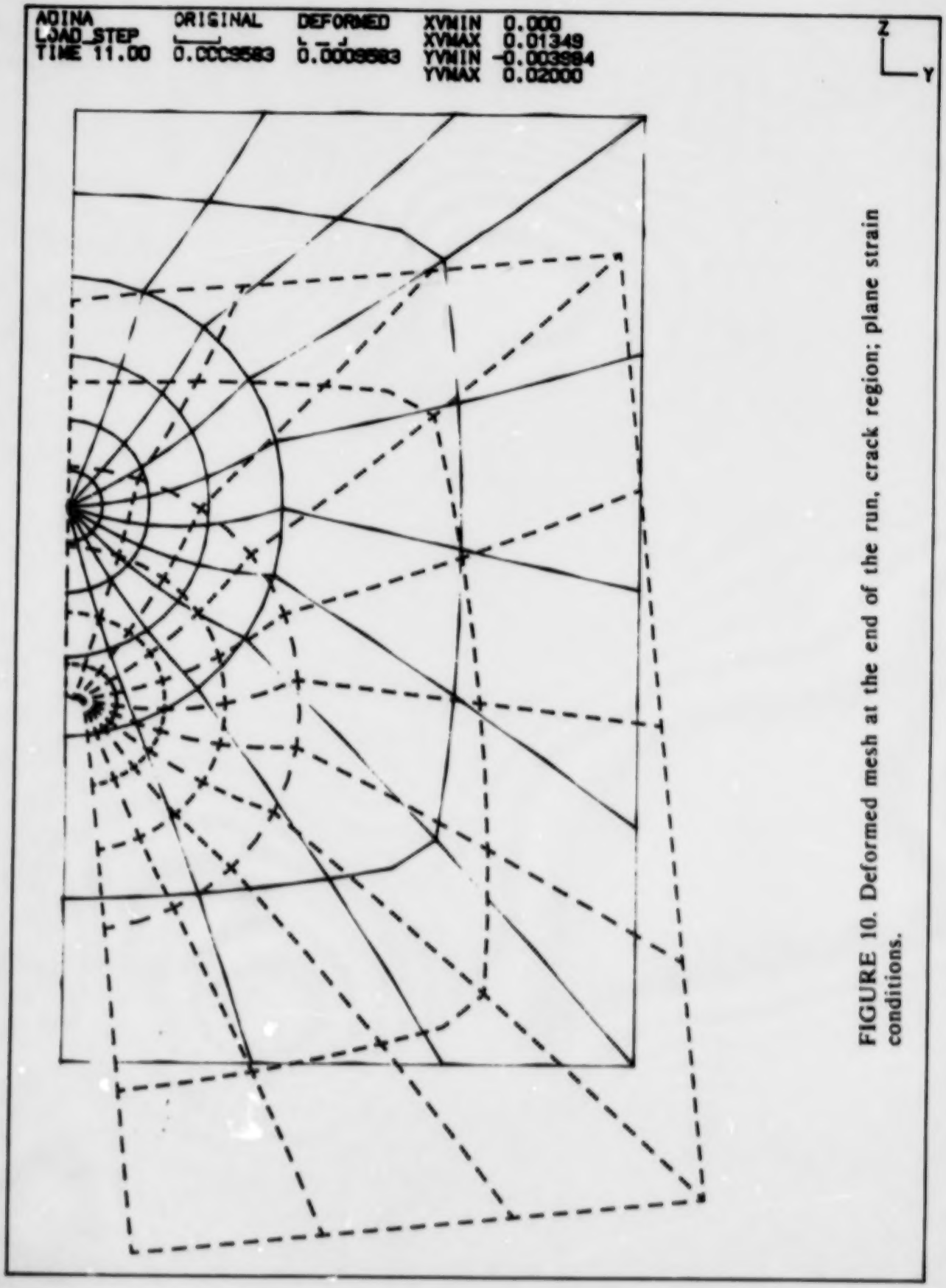

FIGURE 10. Deformed mesh at the end of the run, crack region; plane strain conditions.

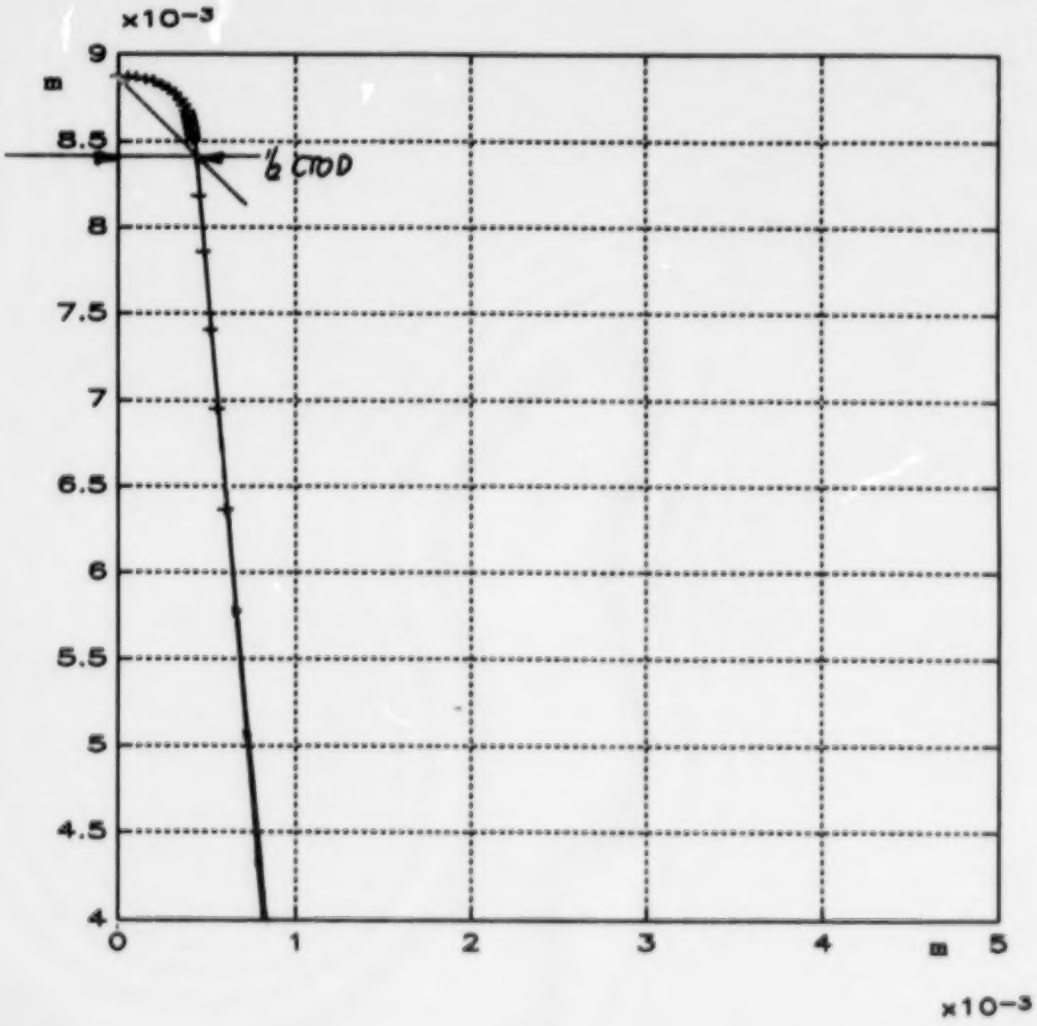

FIGURE 11. Crack tip opening displacement; plane strain conditions.

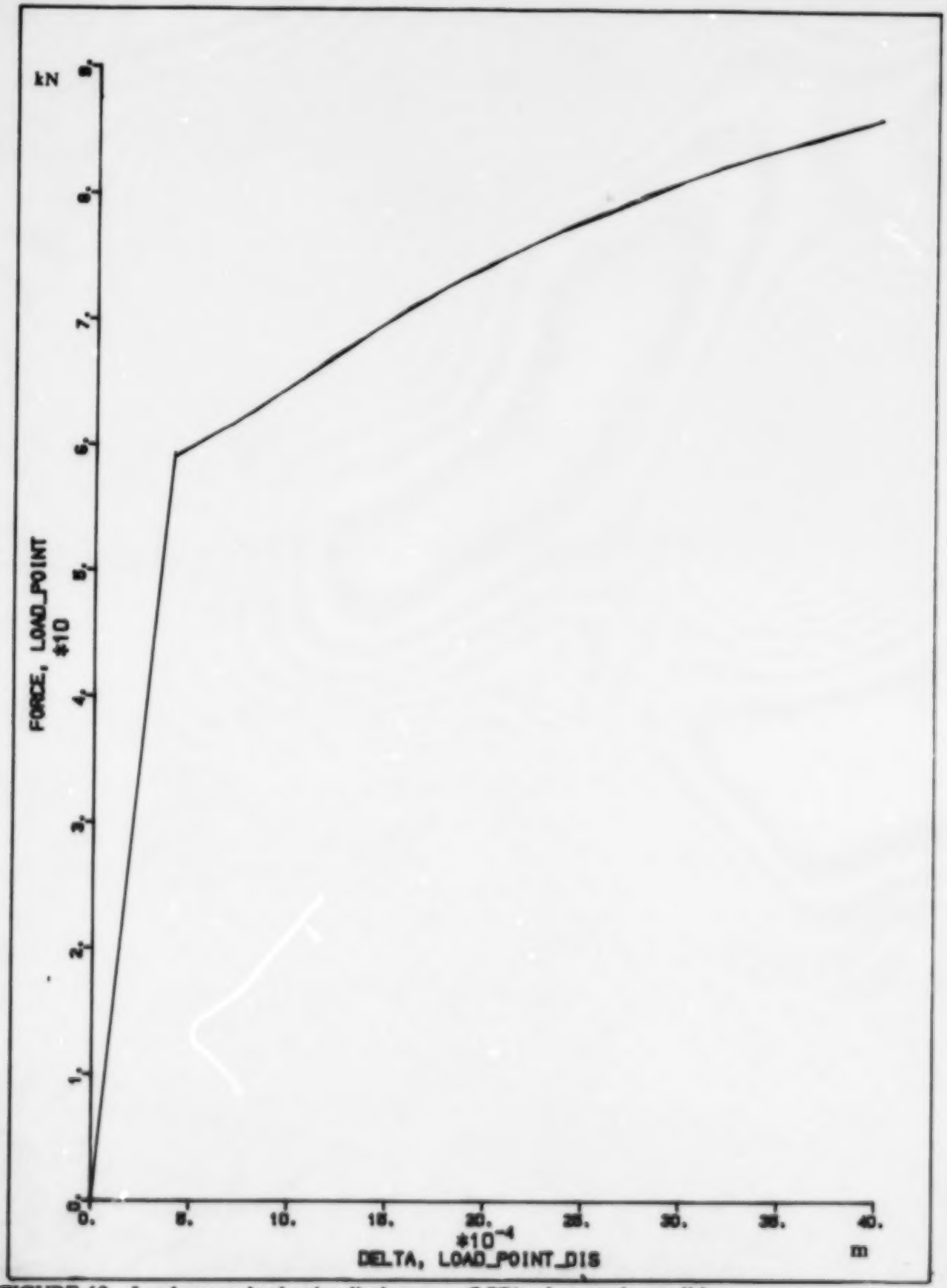

FIGURE 12. Load versus load point displacement (LPD); plane strain conditions.

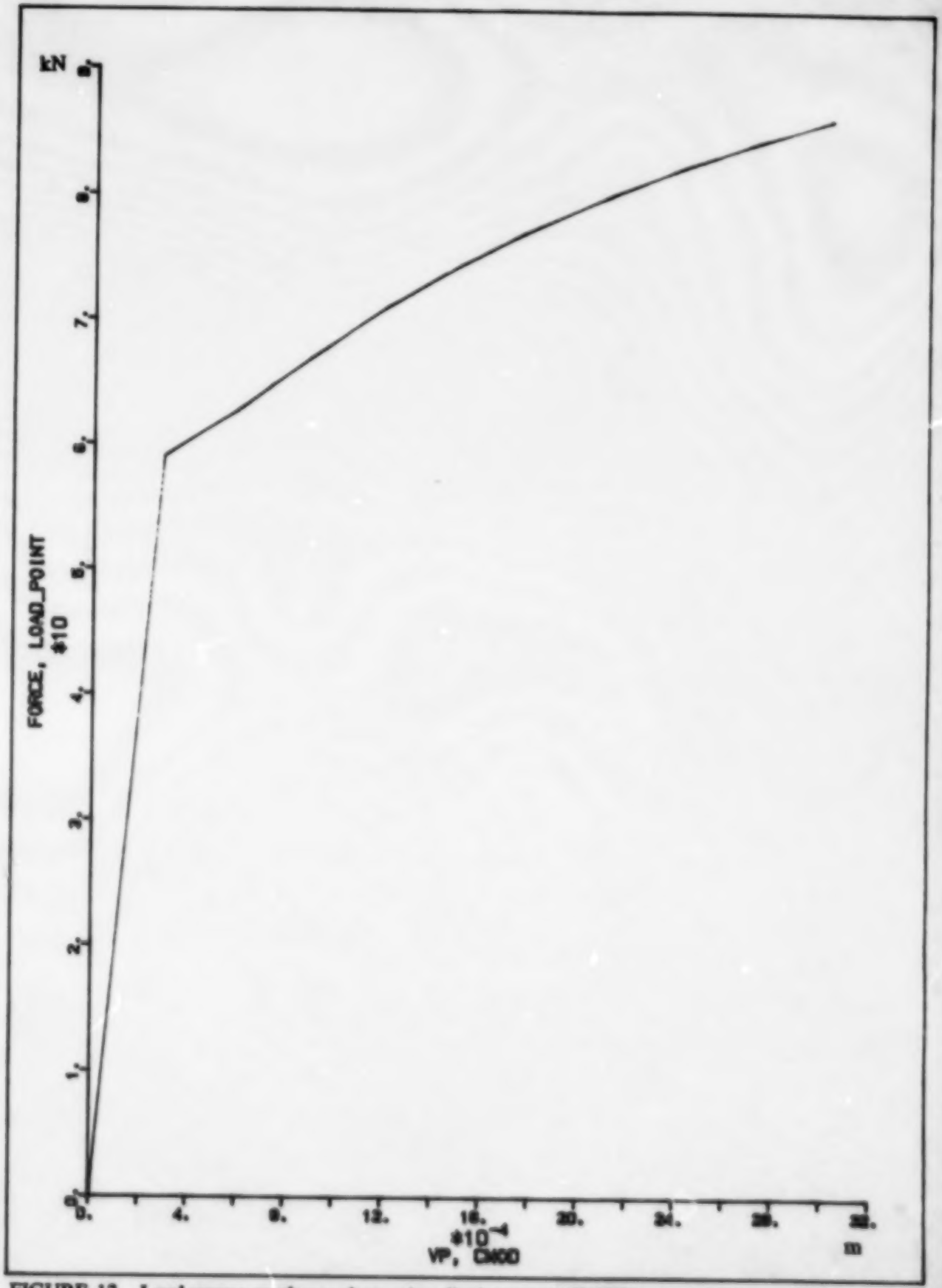

FIGURE 13. Load versus crack mouth opening displacement (CMOD); plane strain conditions.

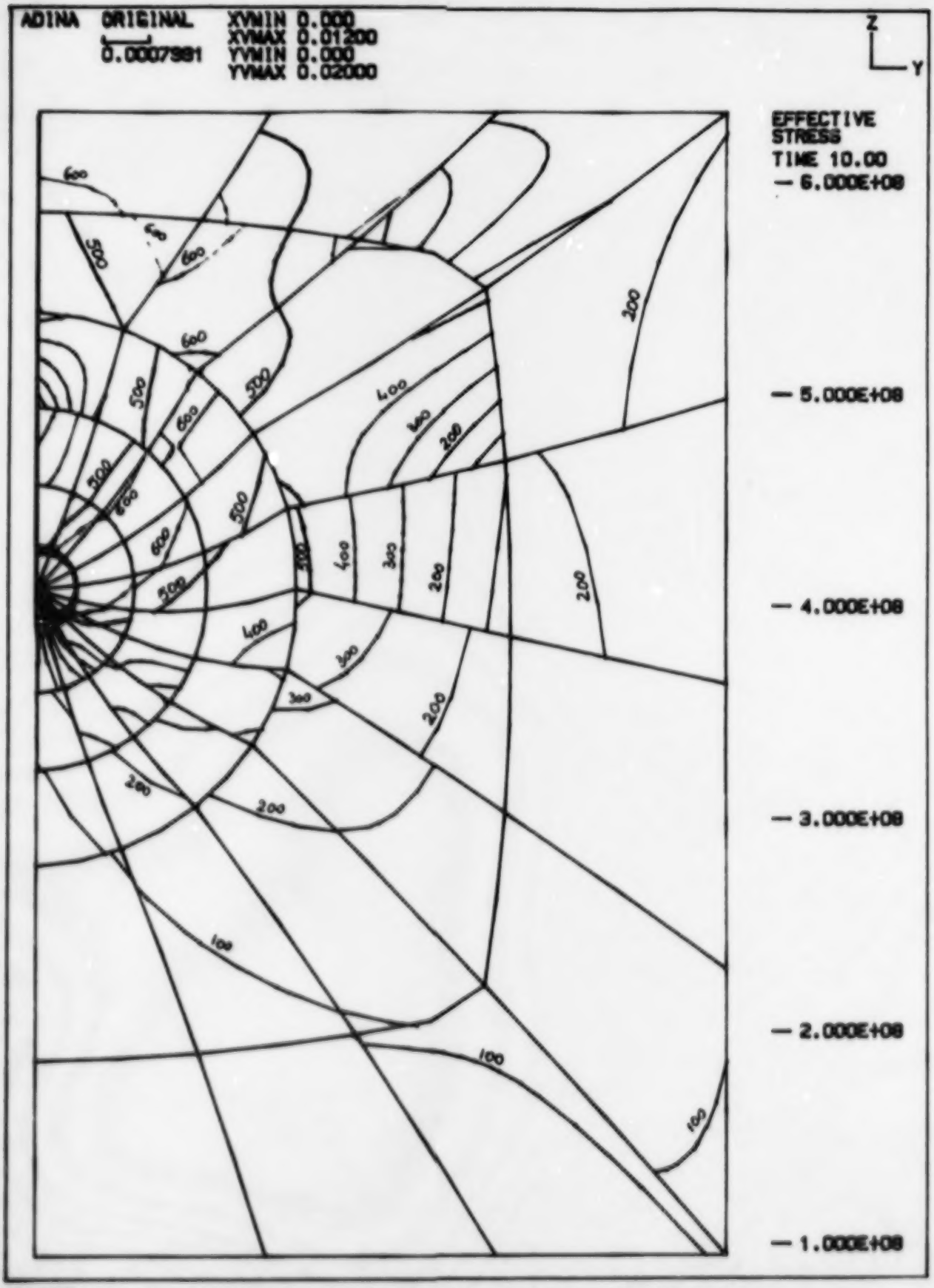

FIGURE 14. Stress distribution under the conditions of plane strain in the specimen.

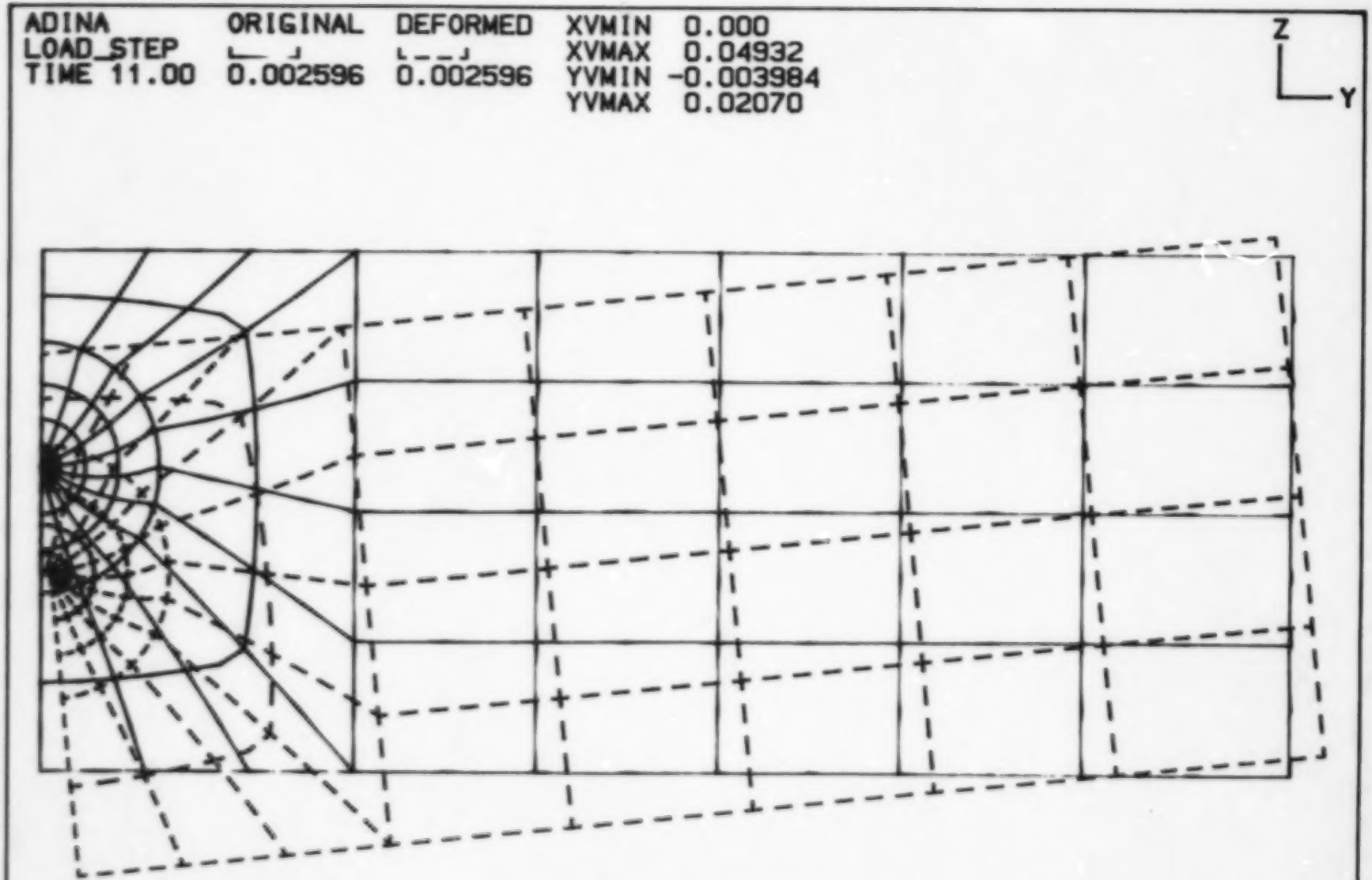

FIGURE 15. Deformed mesh at the end of the run; plane stress conditions.

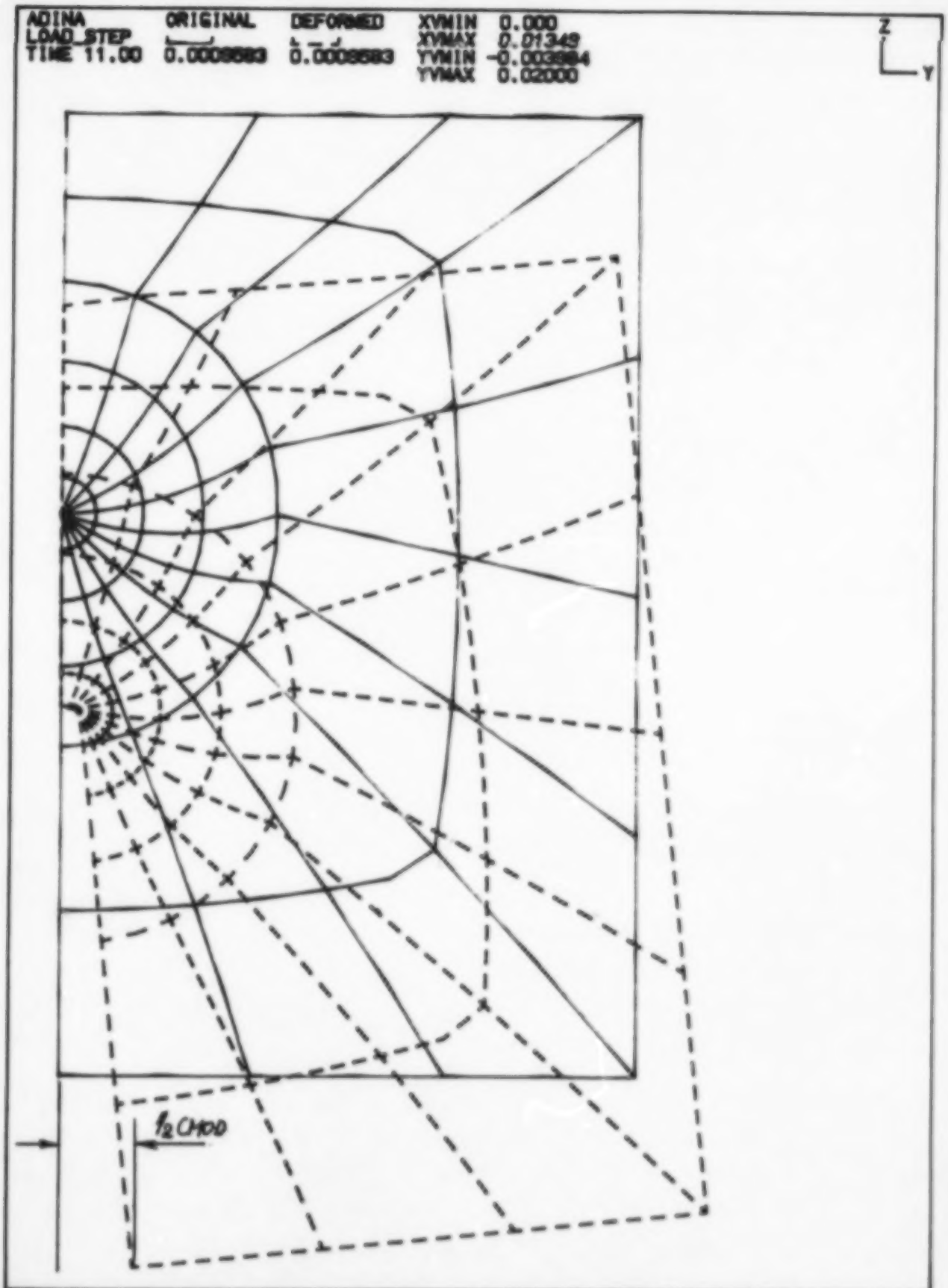

FIGURE 16. Deformed mesh at the end of the run, crack region; plane stress conditions.

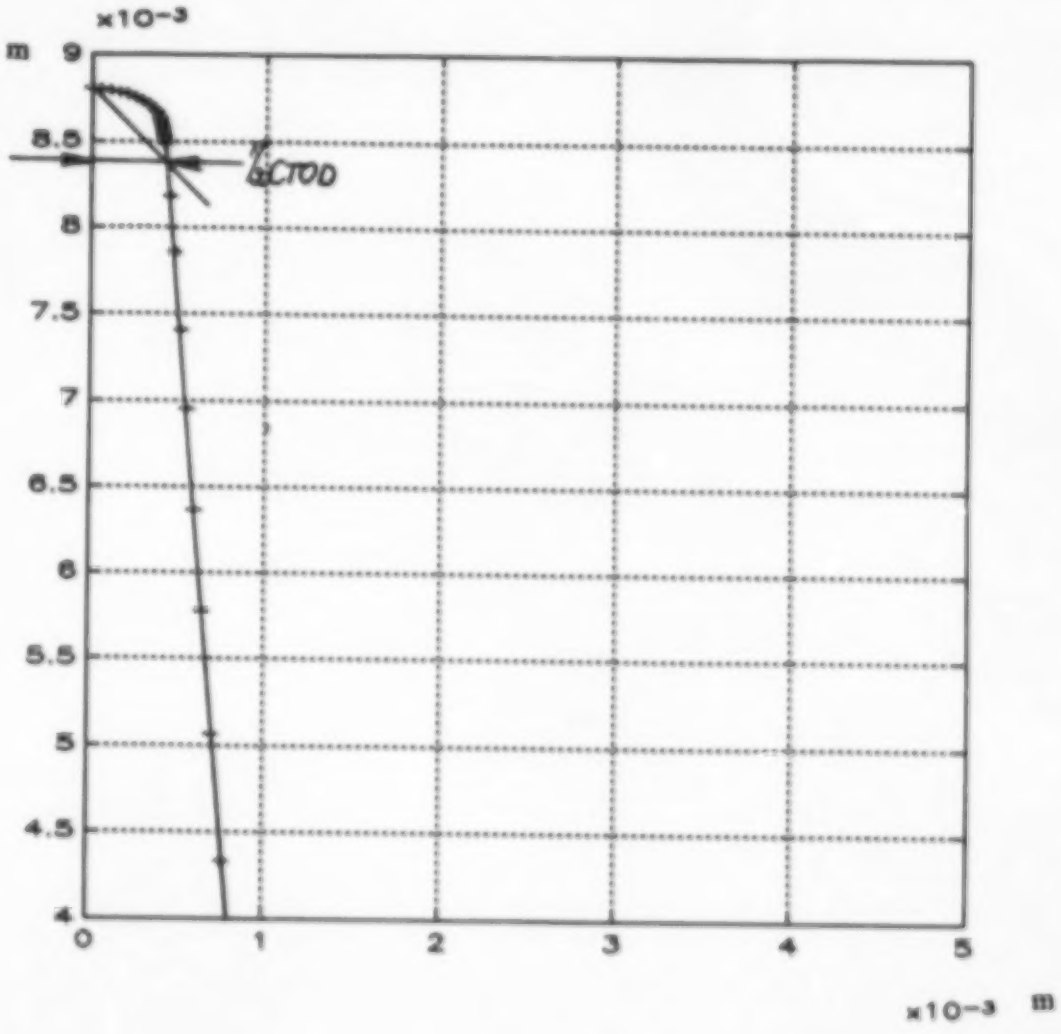

FIGURE 17. Crack tip opening displacement; plane stress conditions.

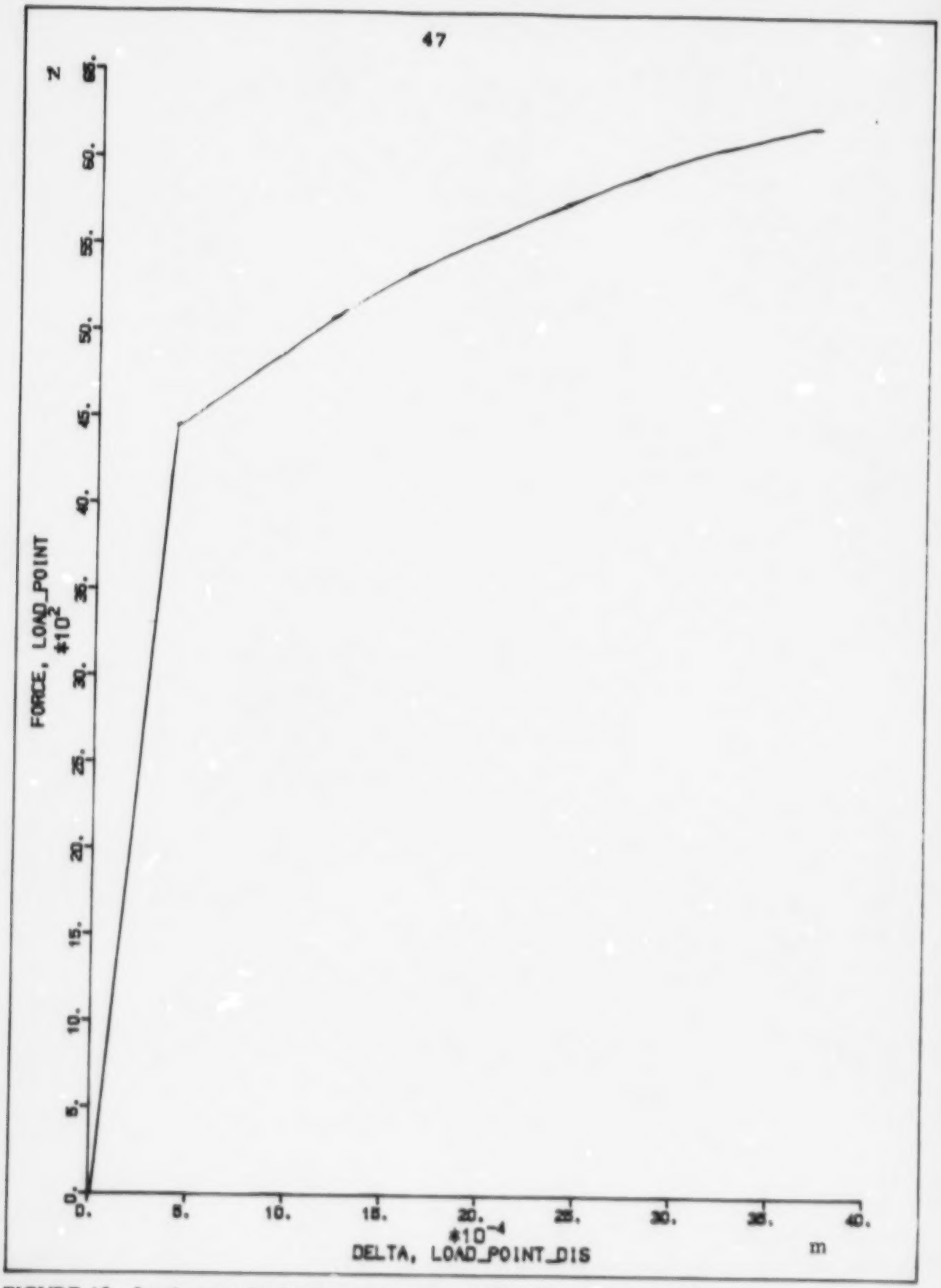

FIGURE 18. Load versus load point displacement (LPD); plane stress conditions.

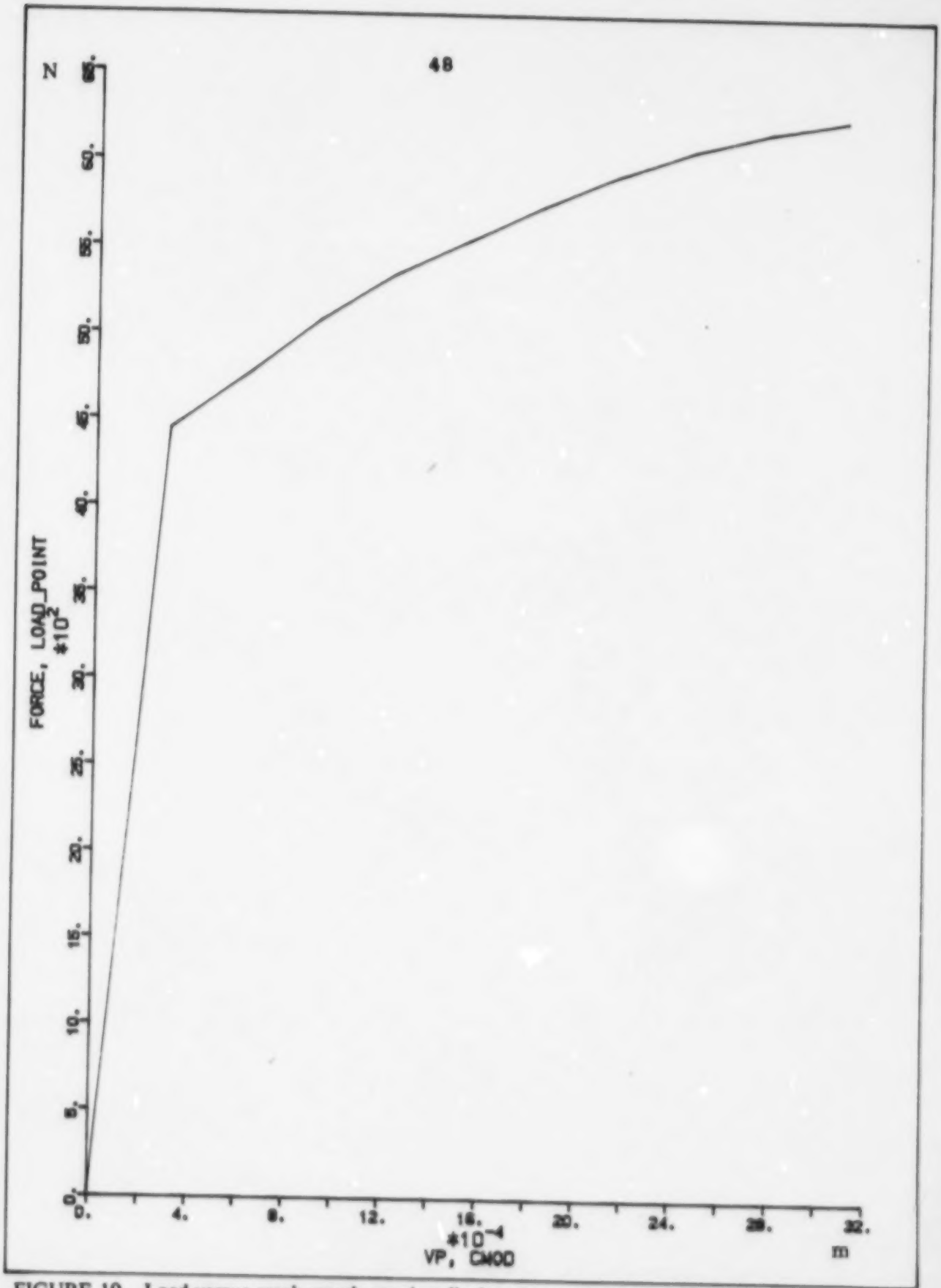

FIGURE 19. Load versus crack mouth opening displacement (CMOD); plane stress conditions.

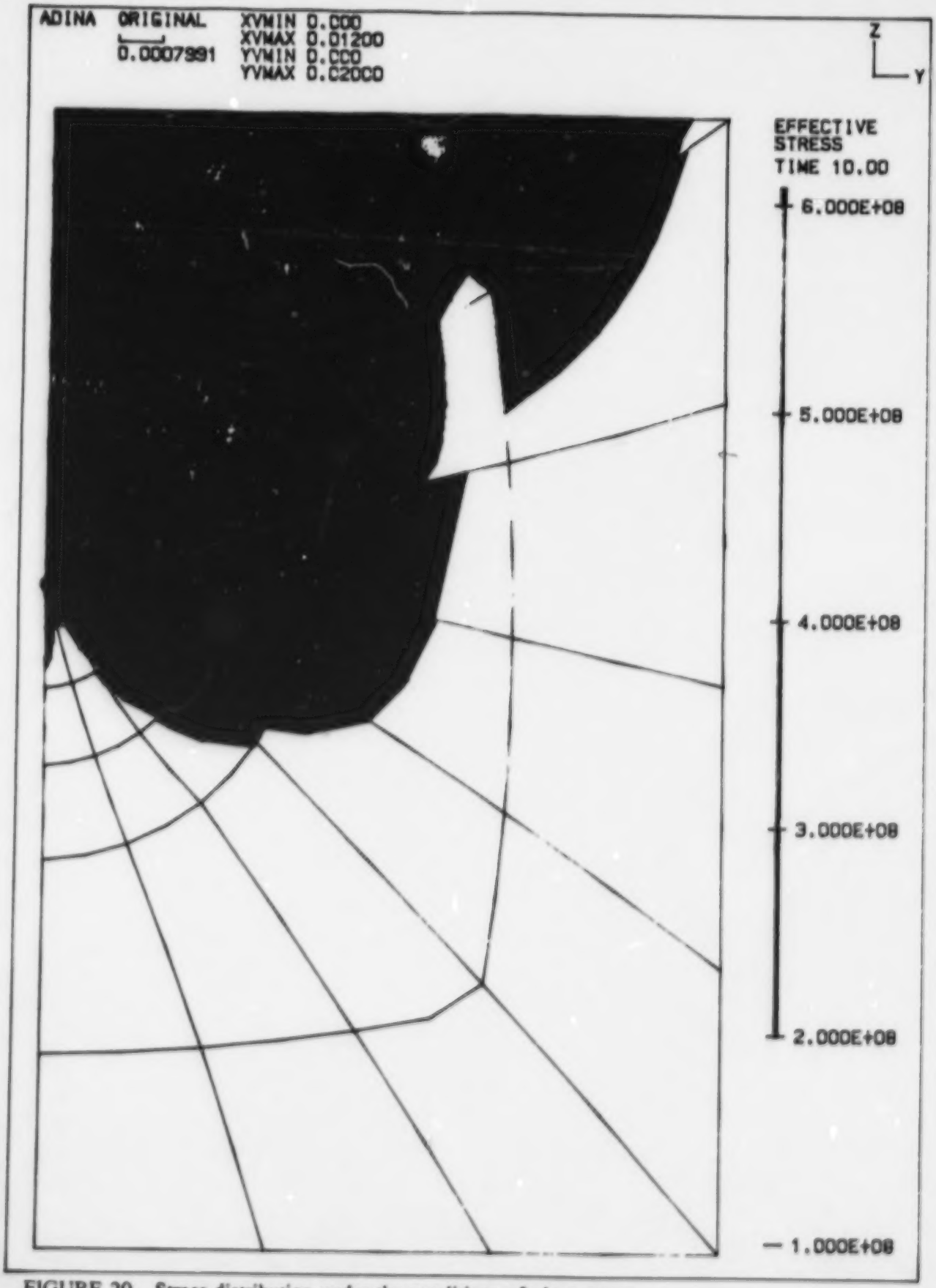

FIGURE 20. Stress distribution under the conditions of plane stress.

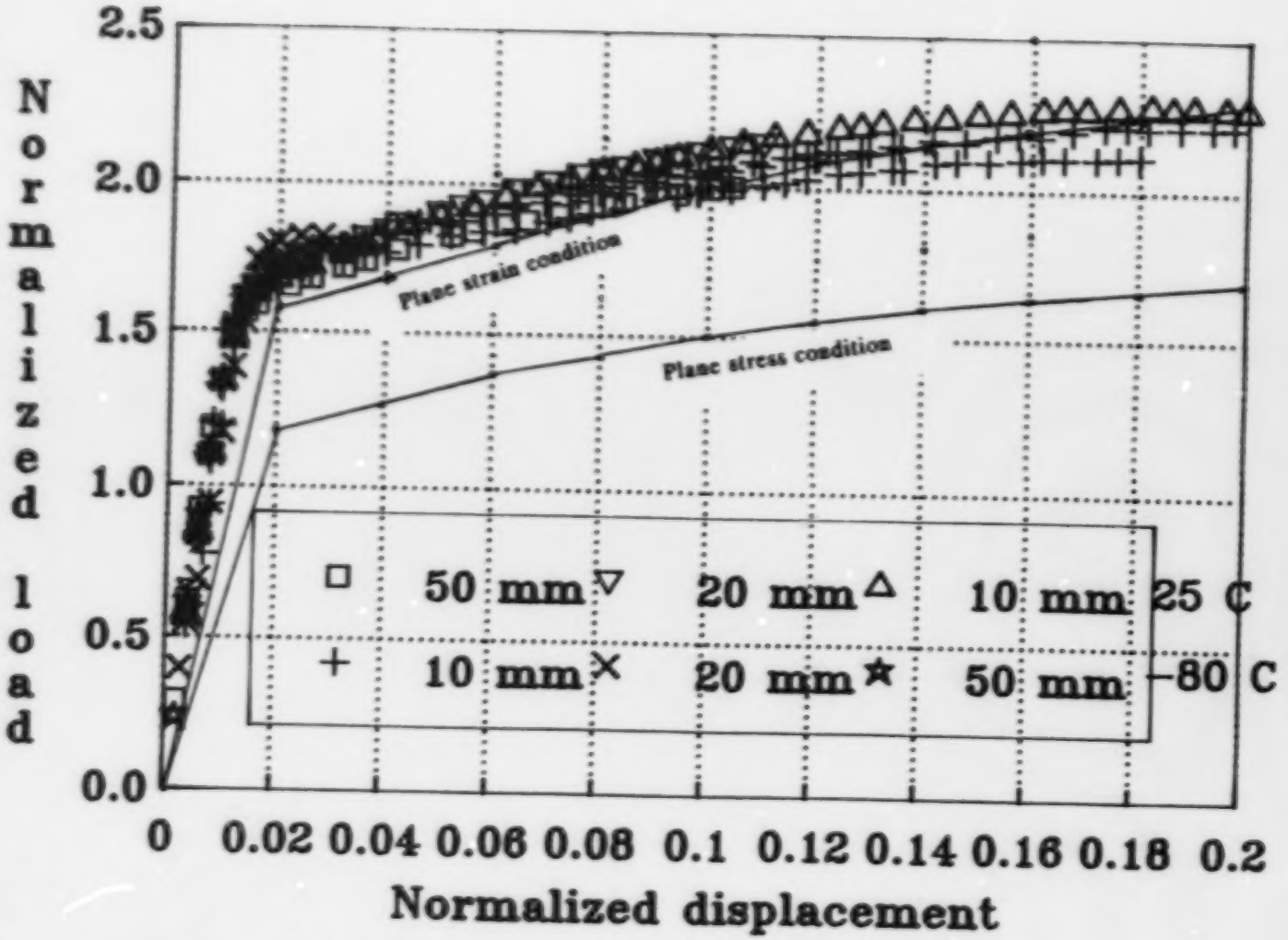

FIGURE 21. Comparison of numerical and experimental results for the three-point-bend specimen.

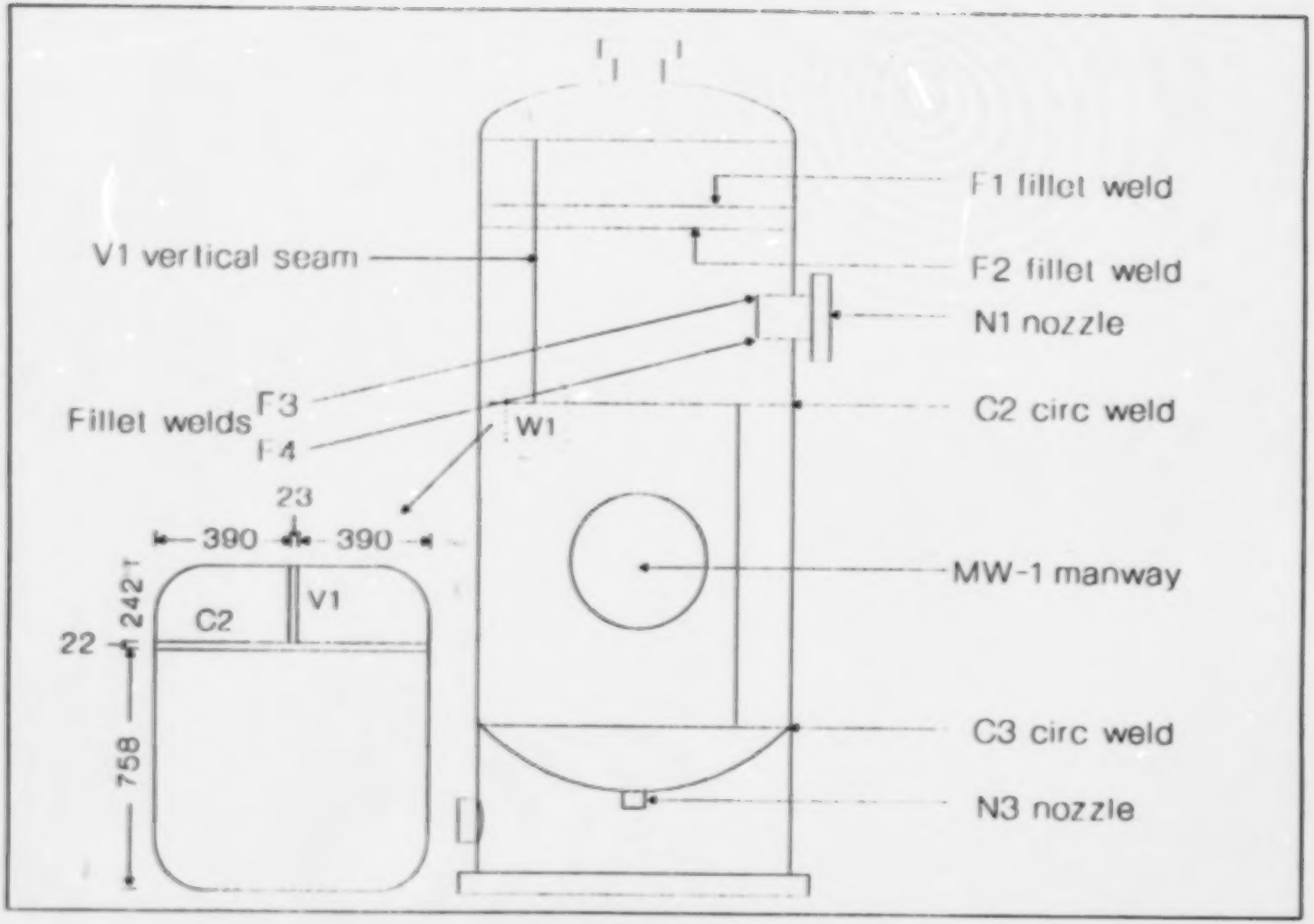

FIGURE 22. Diagram of the pressure vessel.

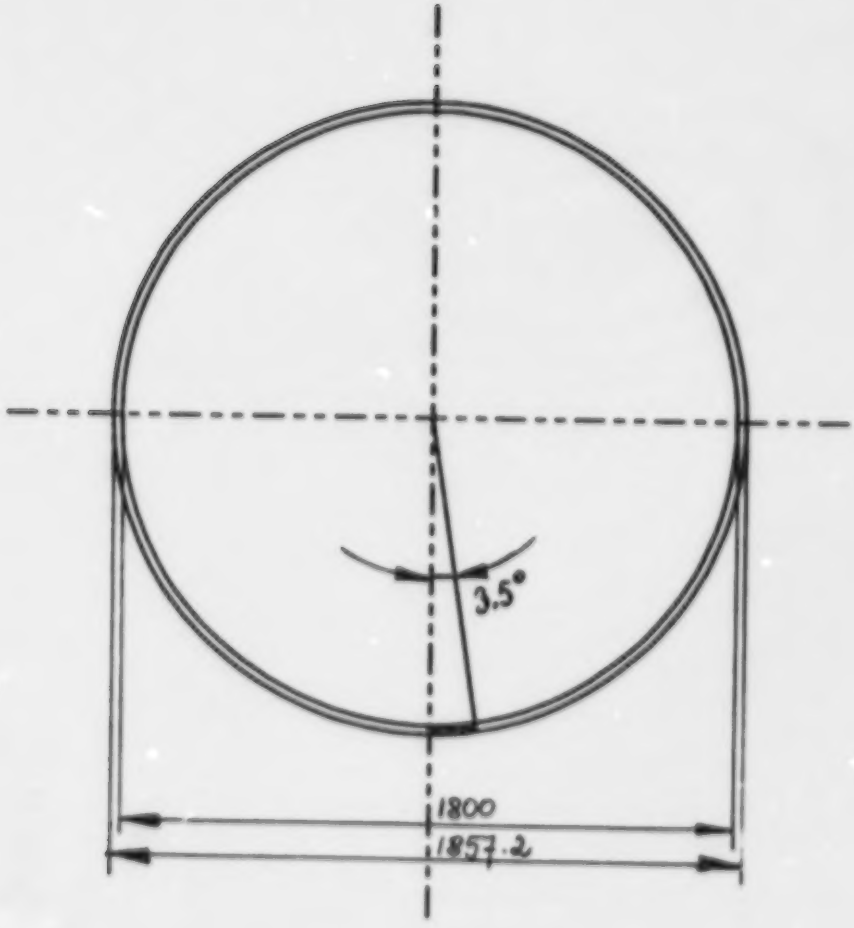

FIGURE 23. Location of the finite element mesh on the circular ring of a pressure vessel.

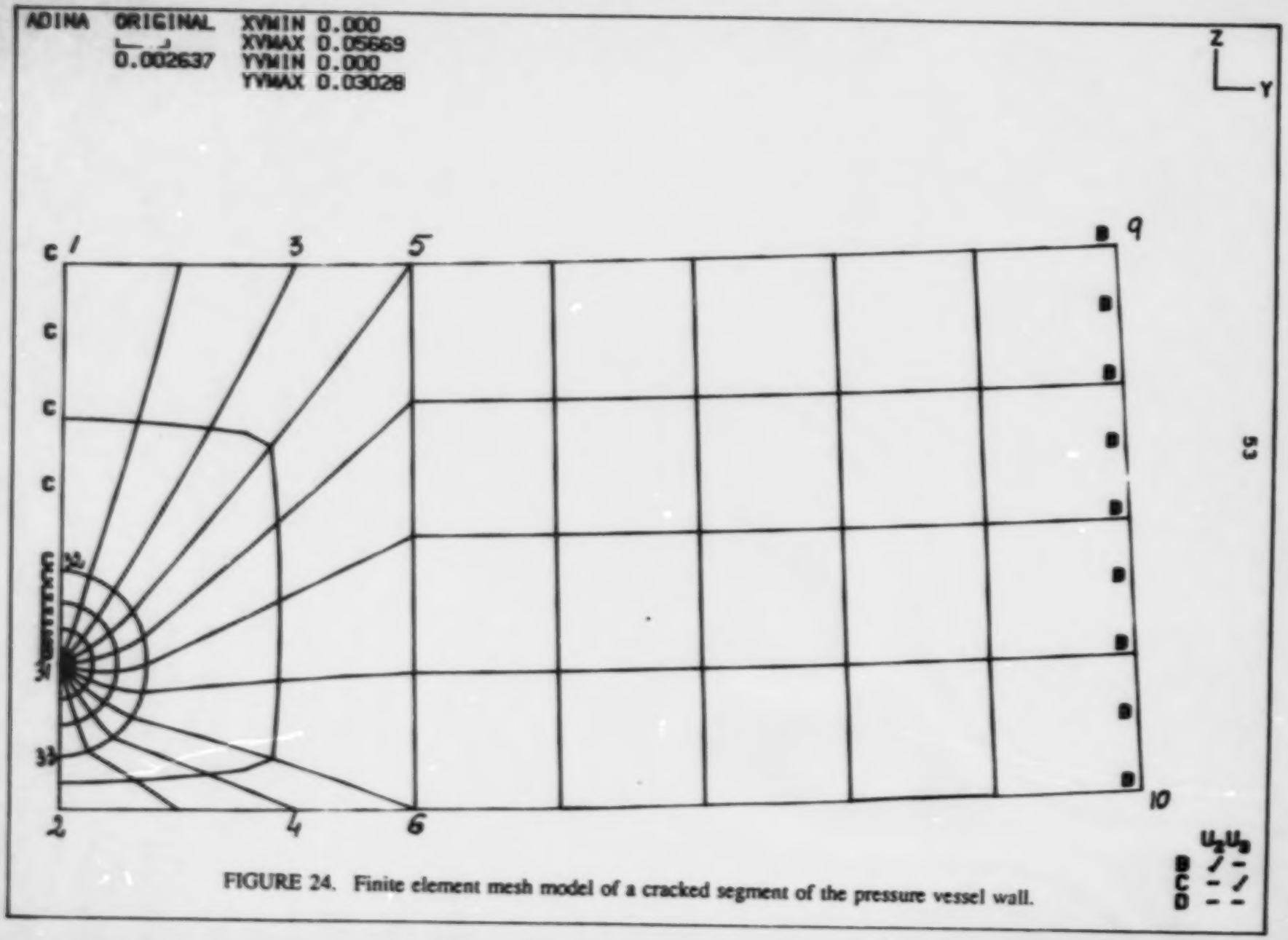

FIGURE 24. Finite element mesh model of a cracked segment of the pressure vessel wall.

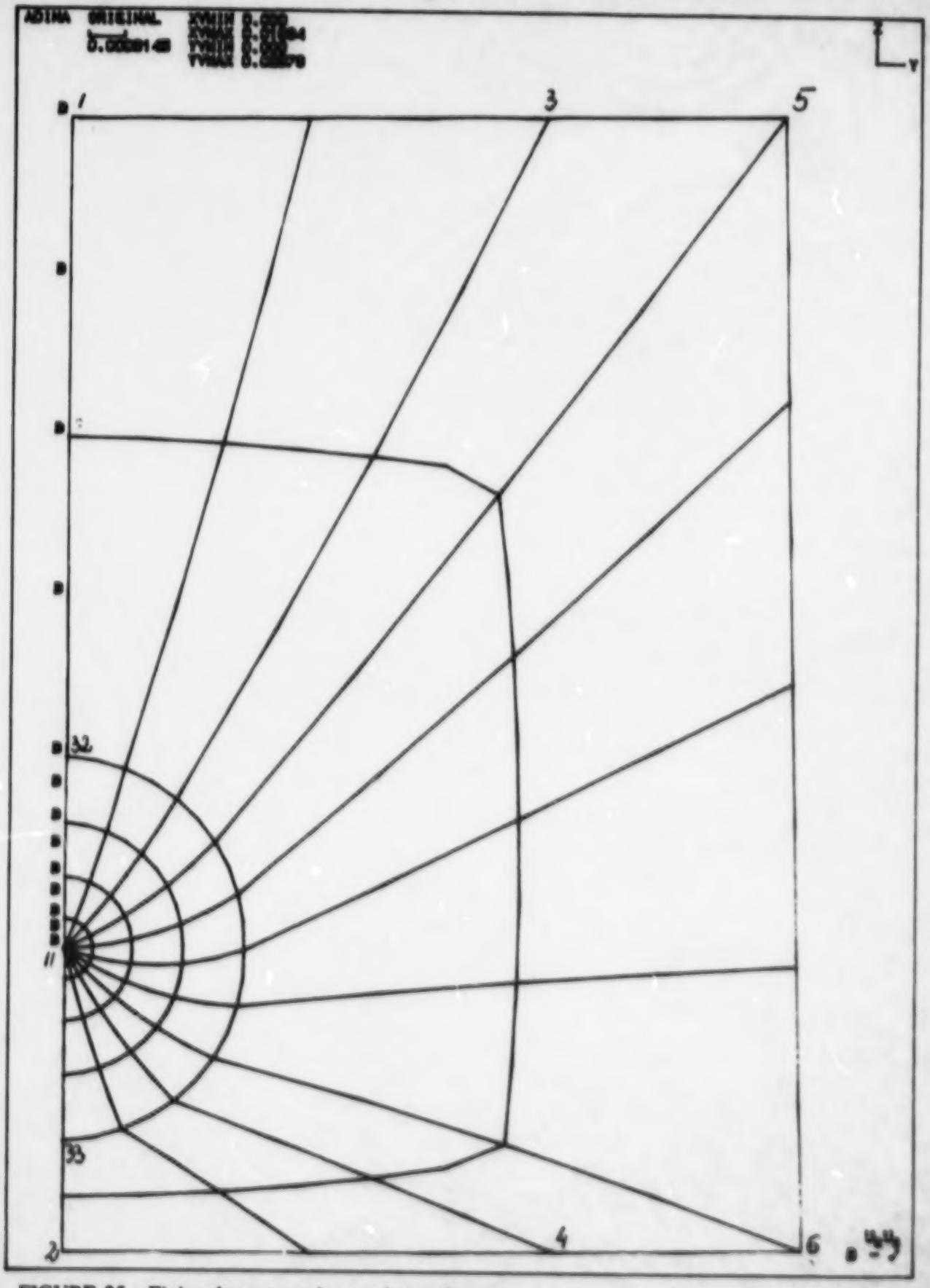

FIGURE 25. Finite element mesh near the crack zone.

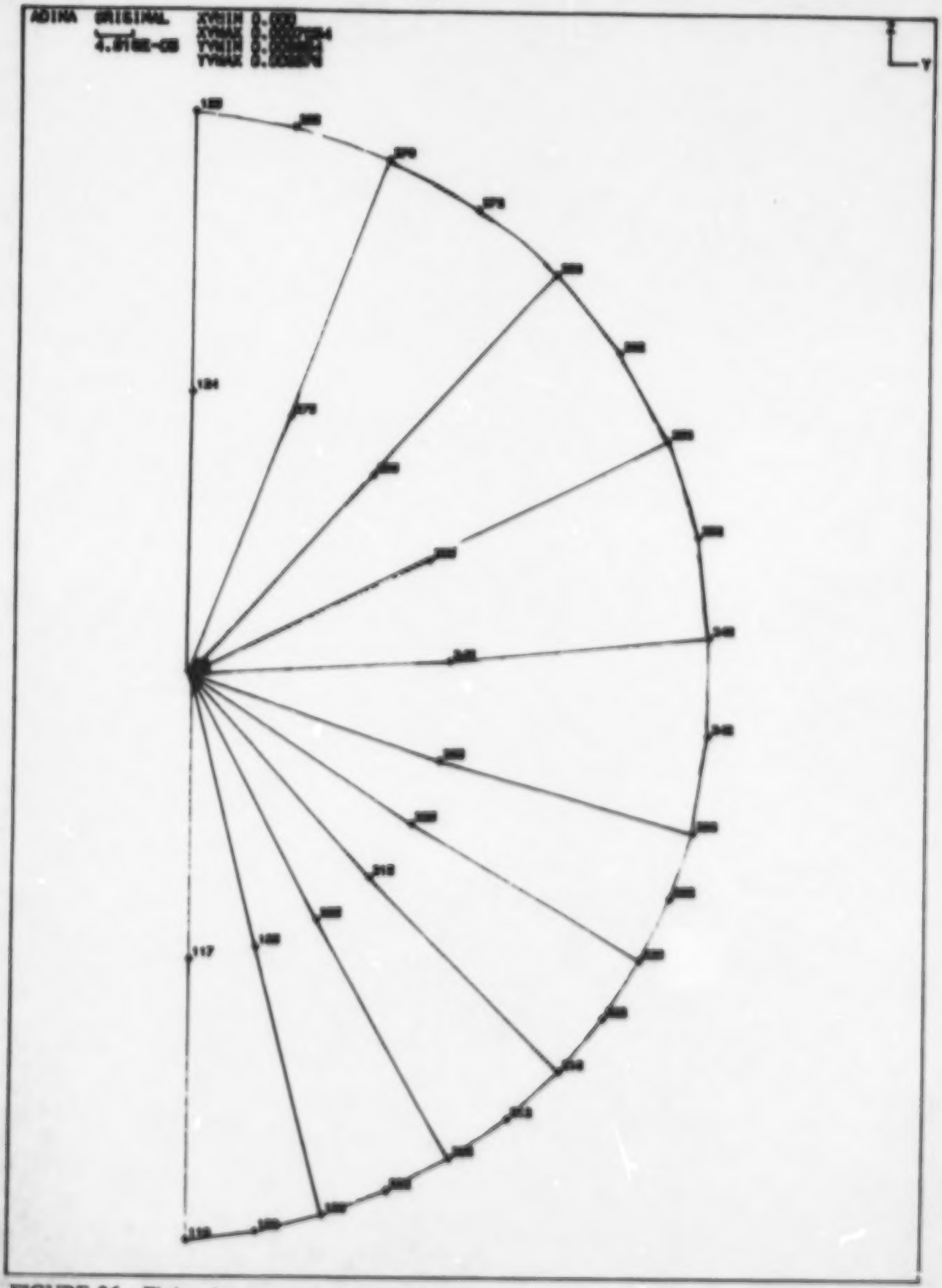

FIGURE 26. Finite element mesh in the crack tip.

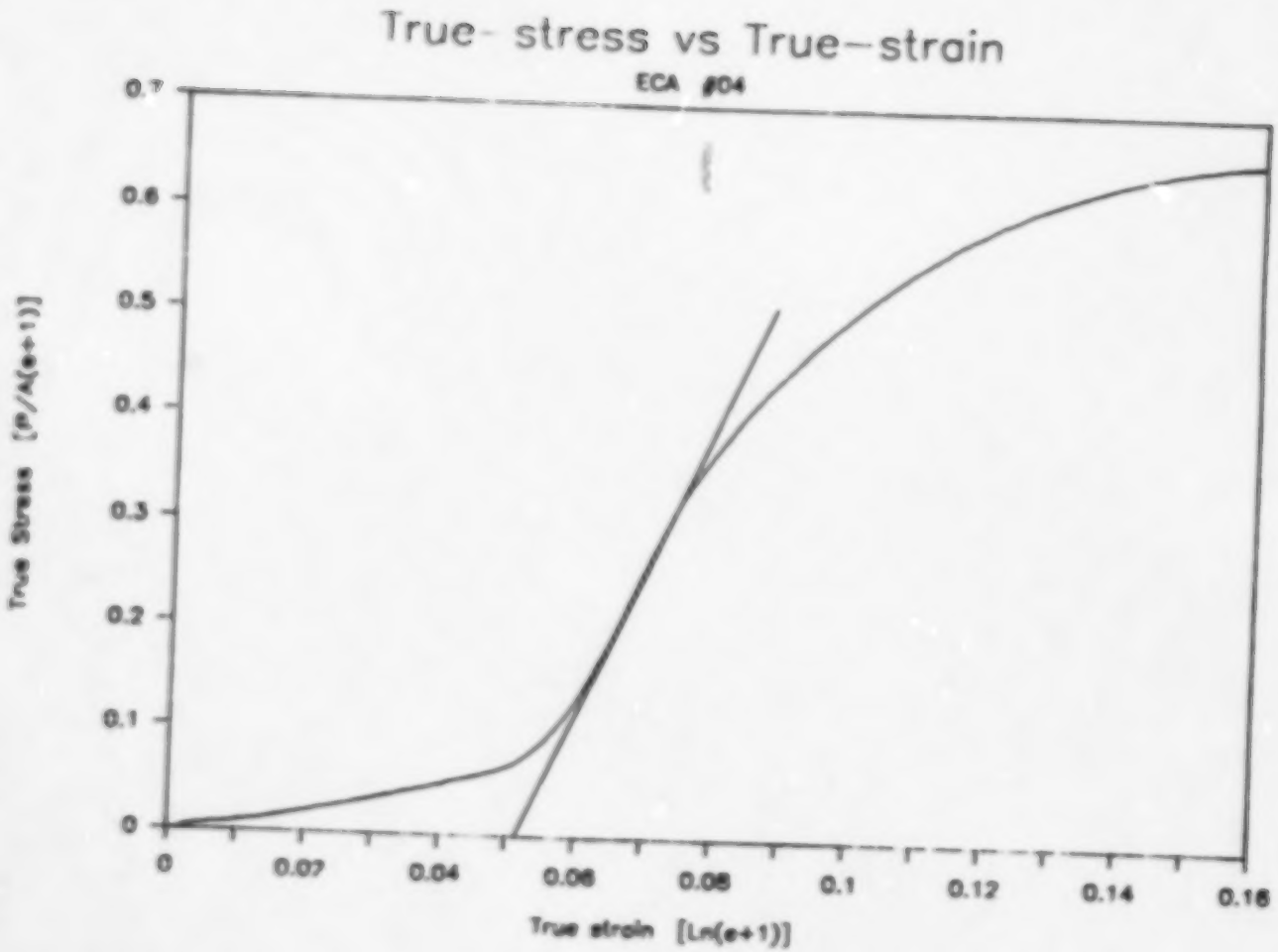

FIGURE 27. Results of experimental testing of the weld material of the pressure vessel. Experiments were carried out in CANMET/MTL.

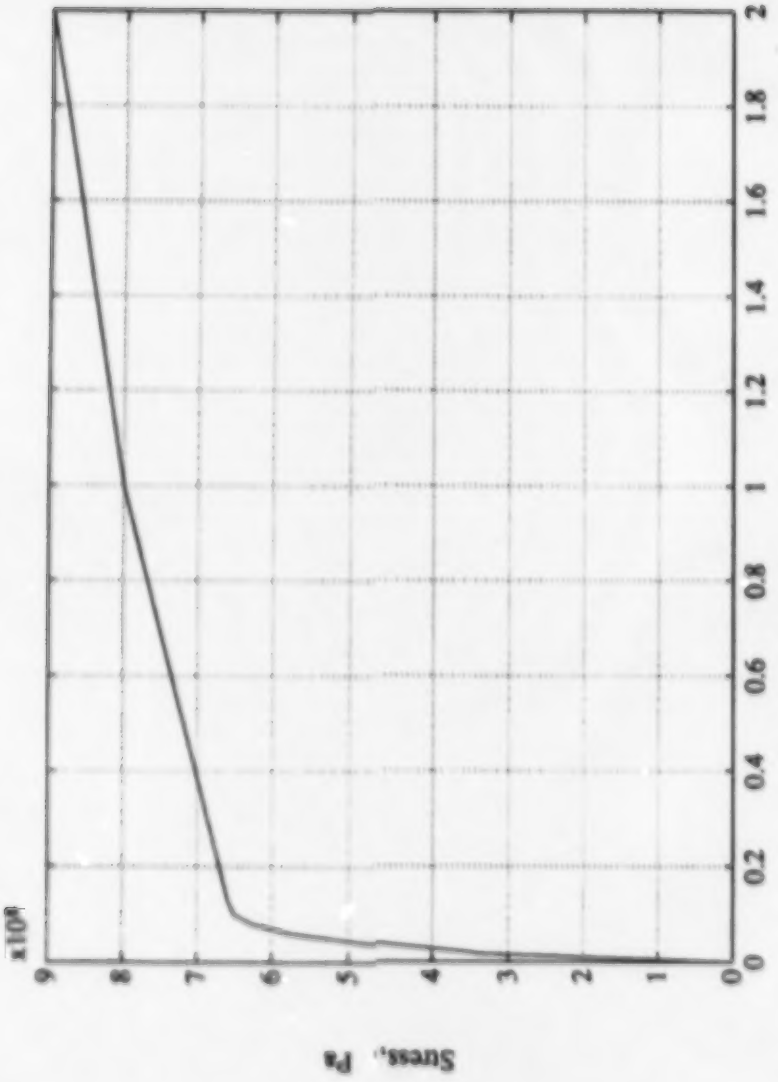

FIGURE 28. Stress-strain curve for the weld material.

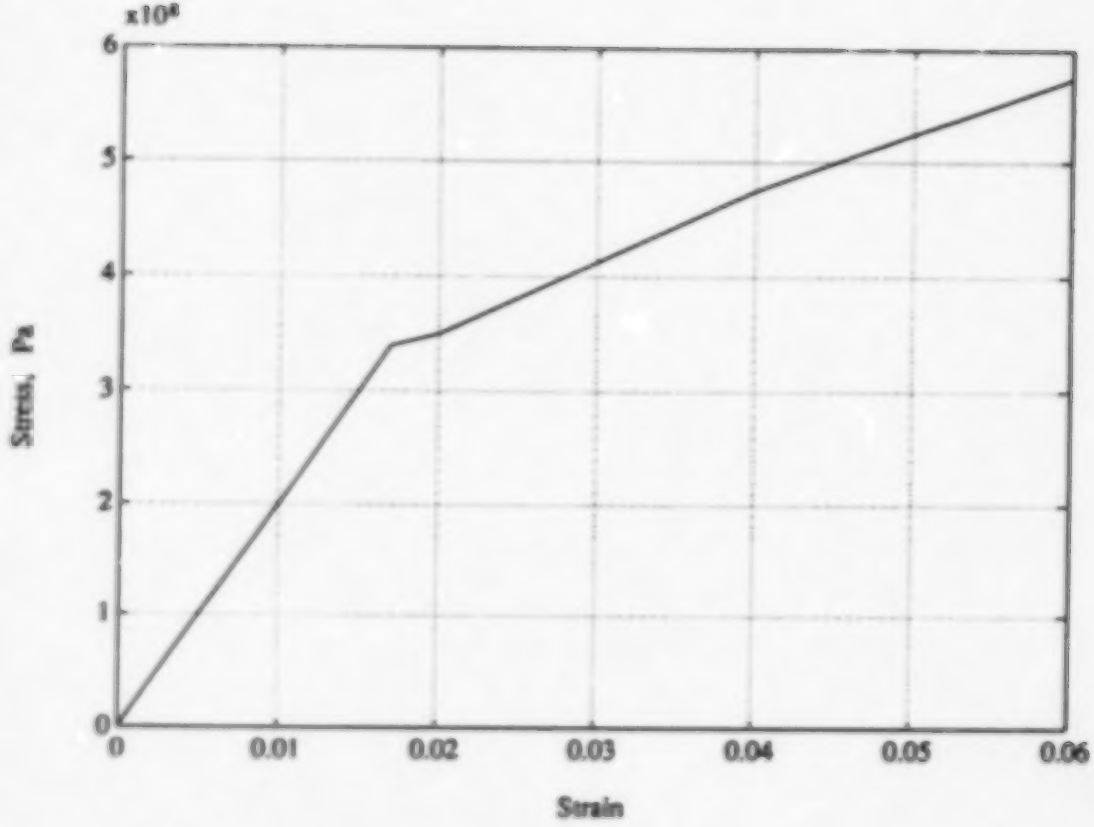

FIGURE 29. Stress-strain curve for the weld material model in the zone of small strains.

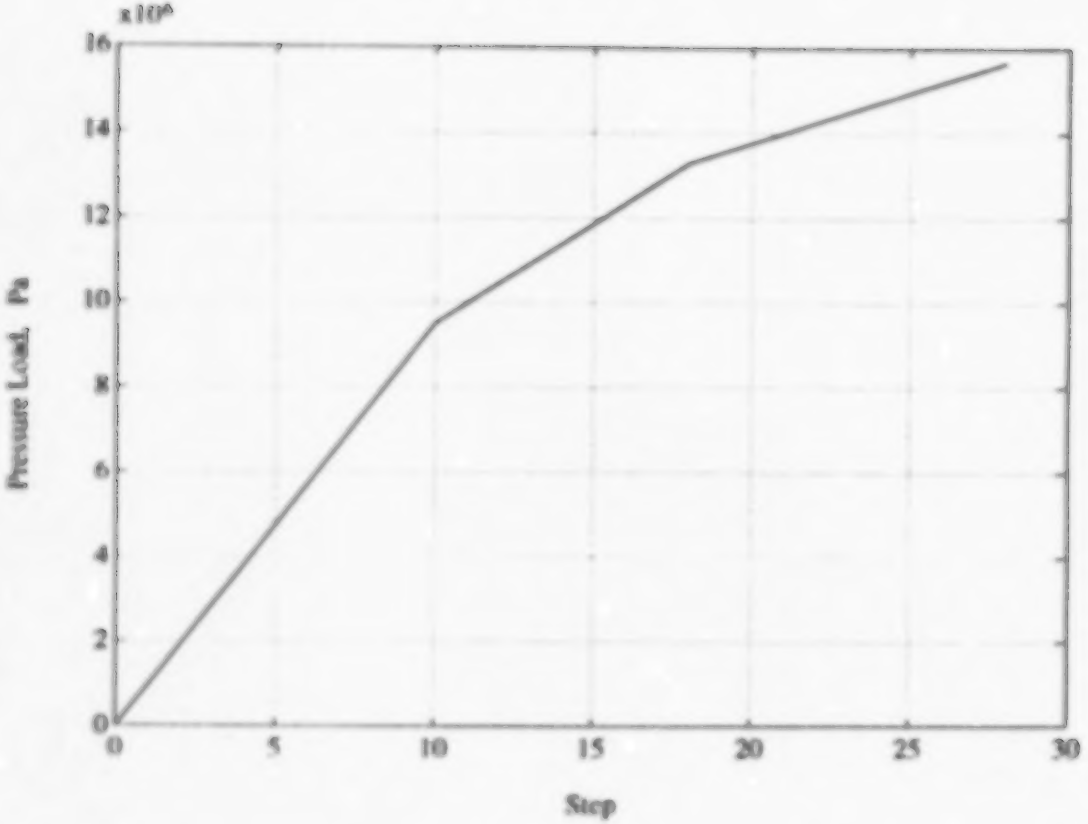

FIGURE 30. Pressure load applied to the cracked pressure-vessel finite element model at each calculation step.

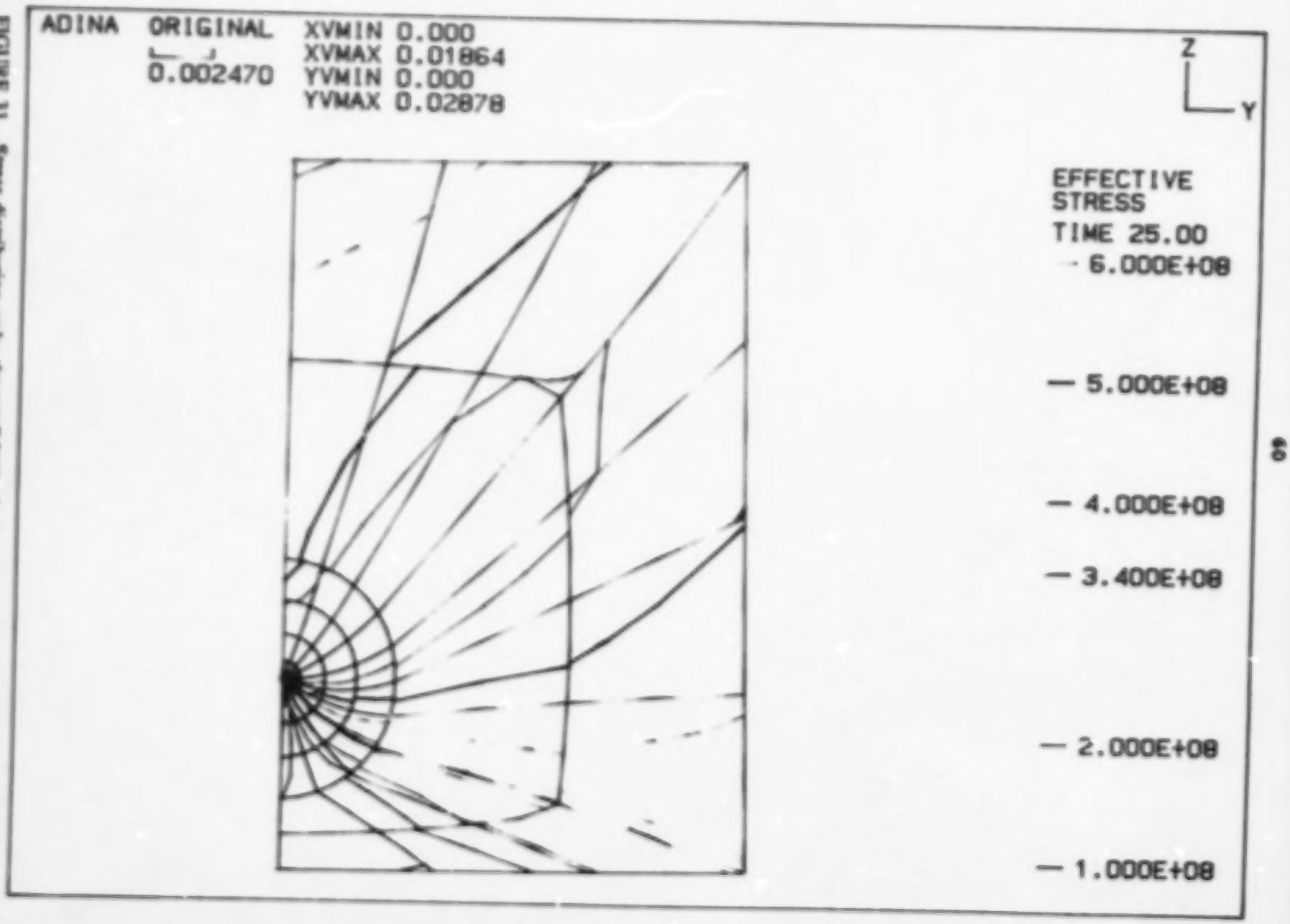

FIGURE 31. Stress distribution under the conditions of plane strain in the ligament.

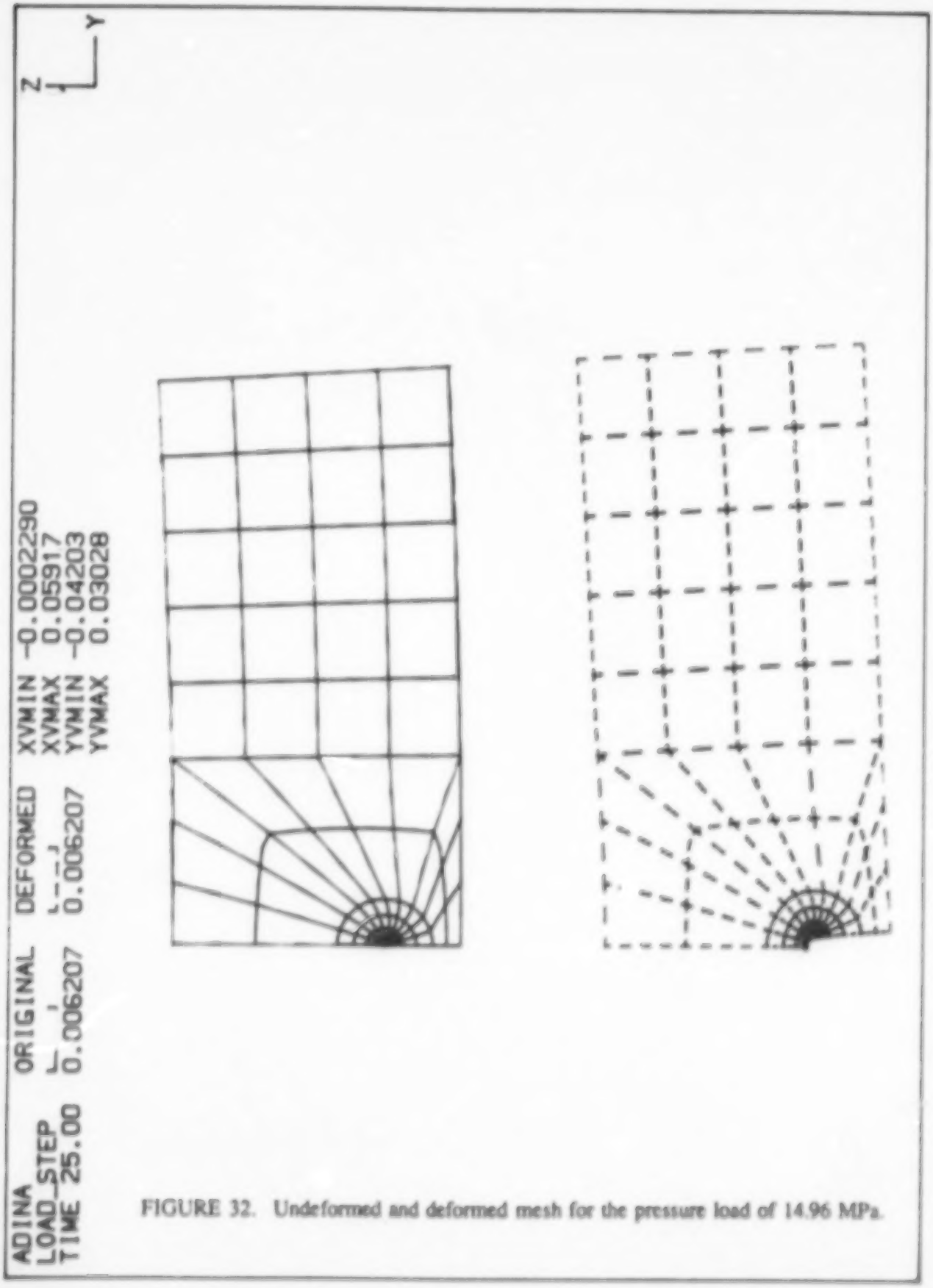

FIGURE 32. Undeformed and deformed mesh for the pressure load of 14.96 MPa.

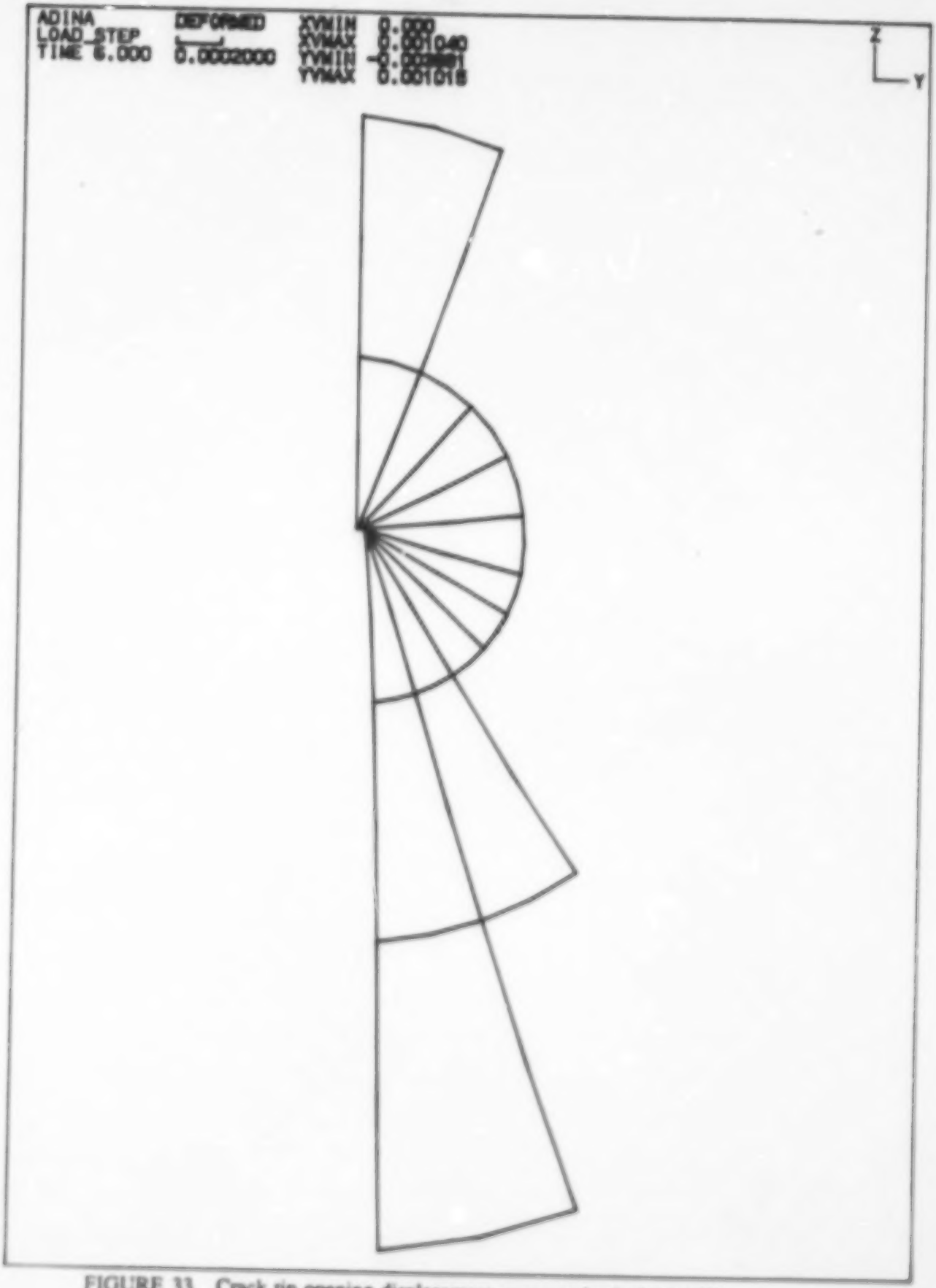

FIGURE 33. Crack tip opening displacement; pressure load of 5.7 MPa.

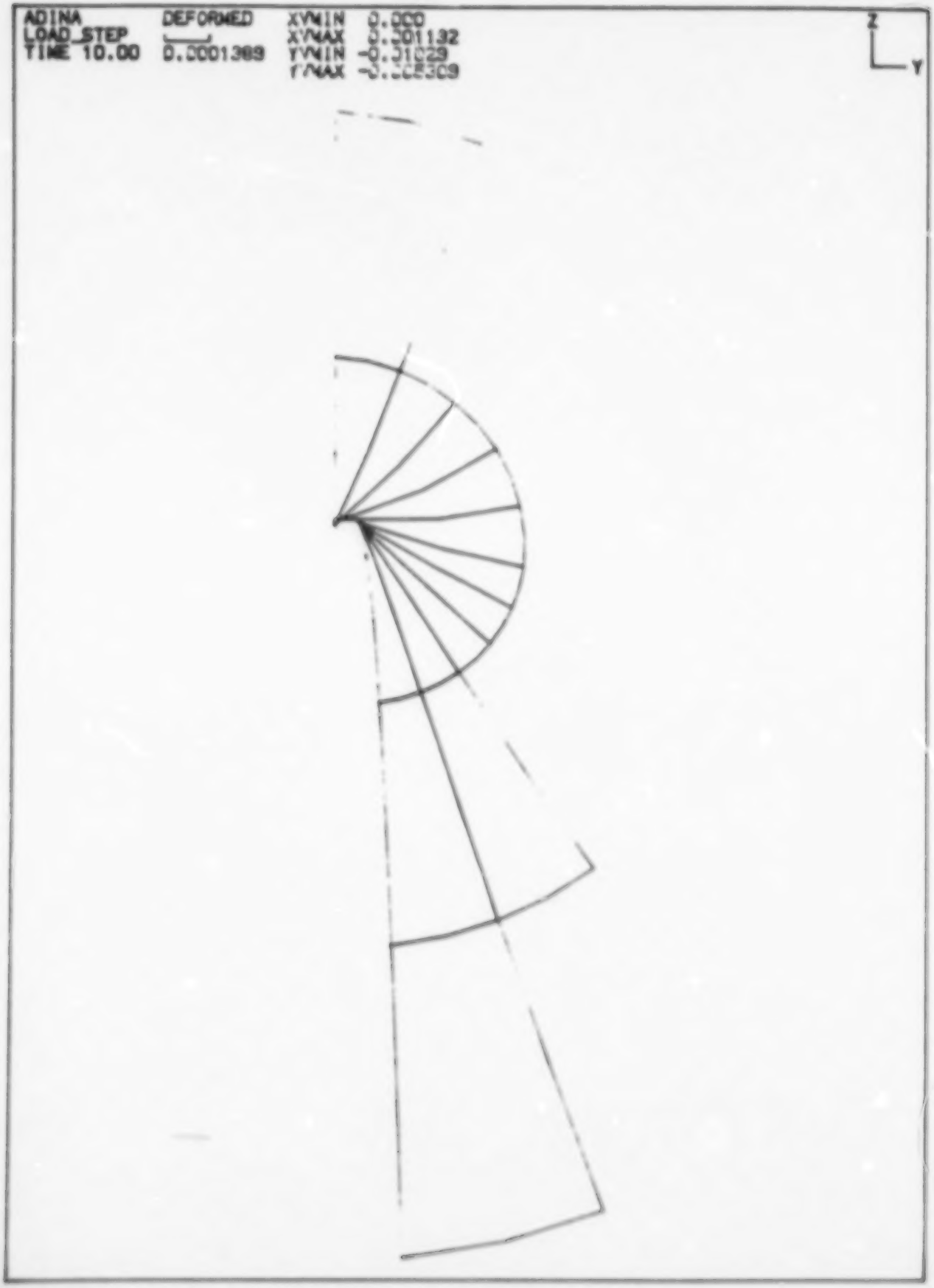

FIGURE 34. Crack tip opening displacement; pressure load of 9.5 MPa.

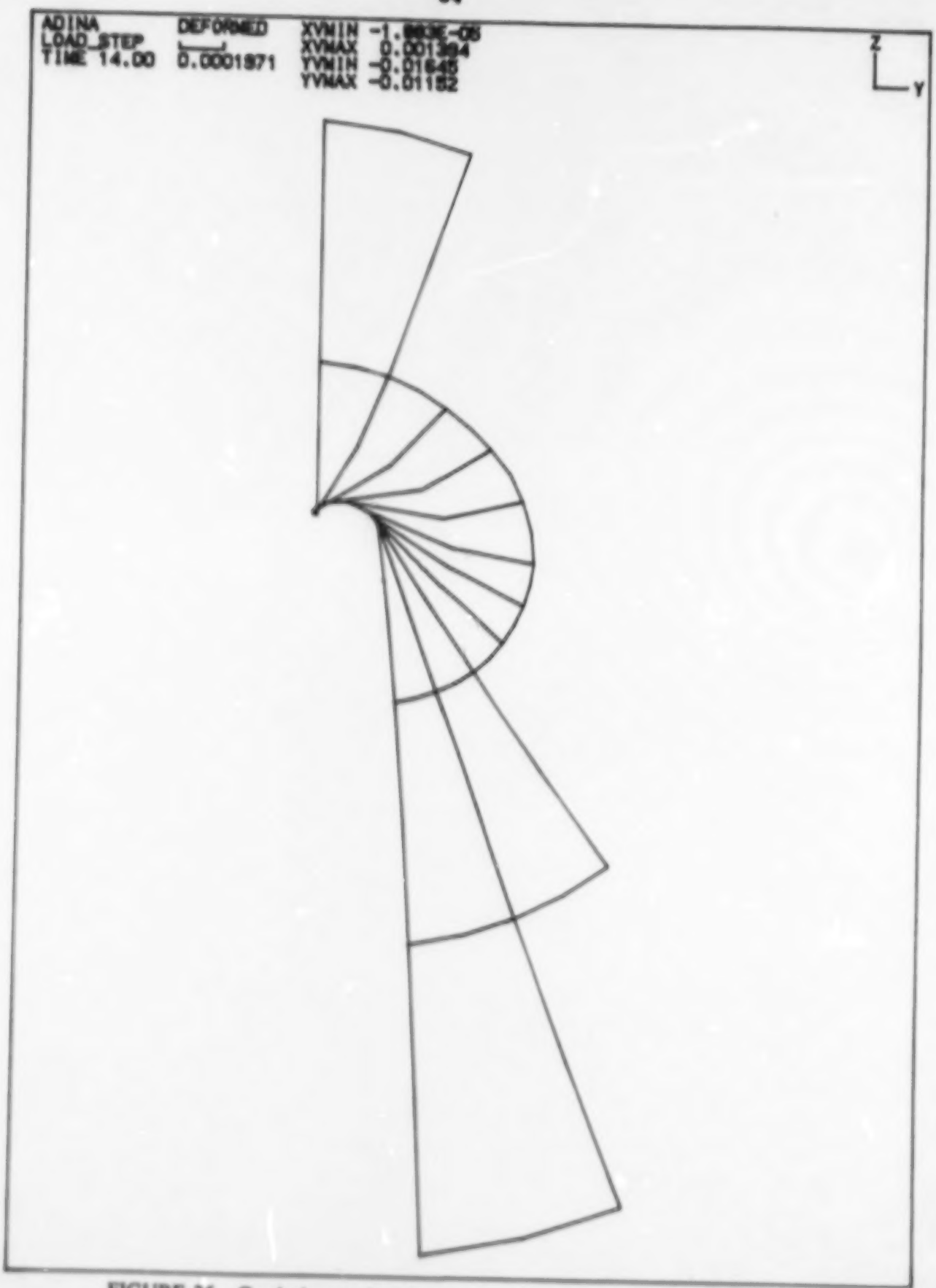

FIGURE 35. Crack tip opening displacement; pressure load of 11.4 MPa.

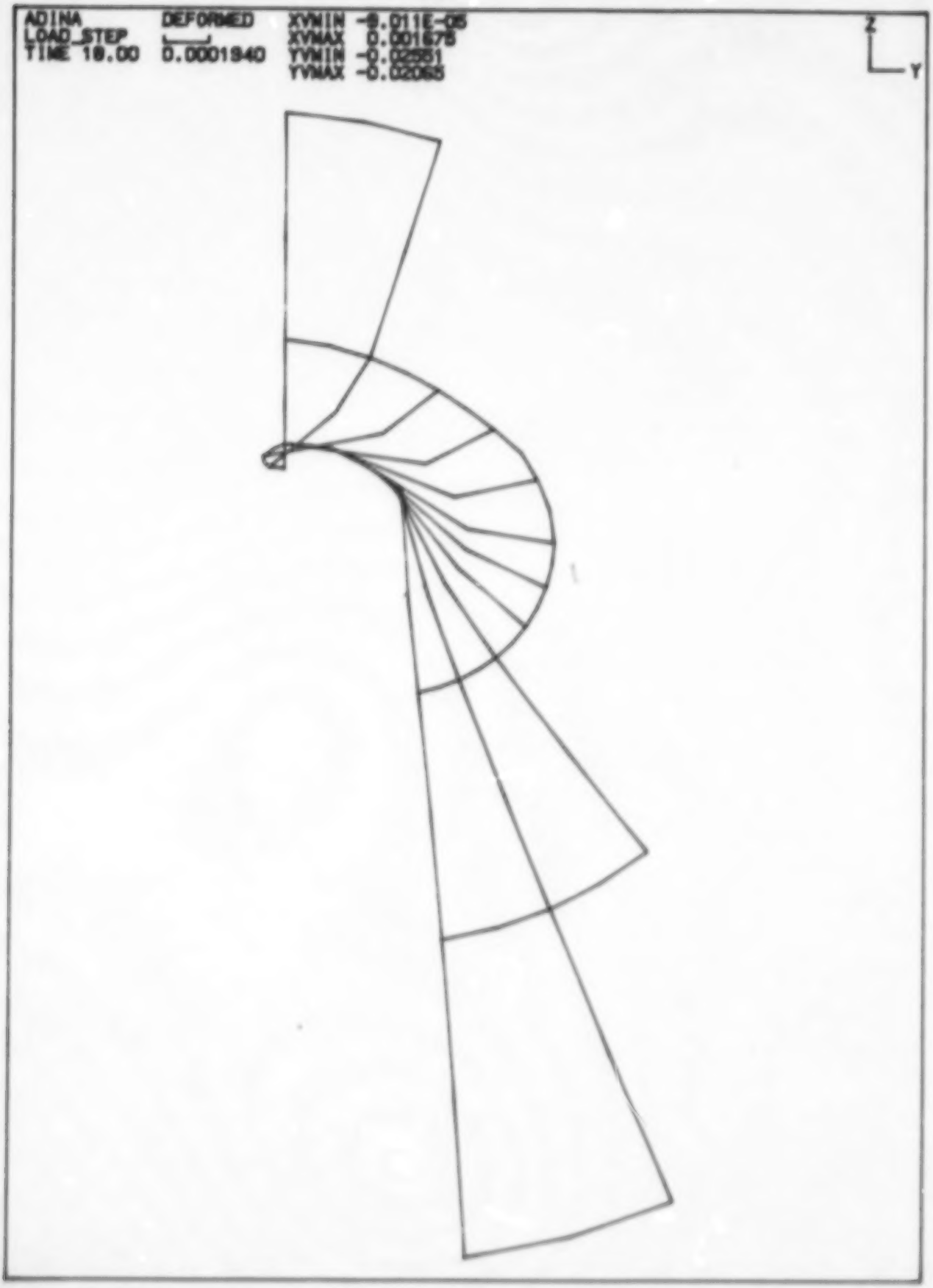

FIGURE 36. Crack tip opening displacement; pressure load of 13.3 MPa.

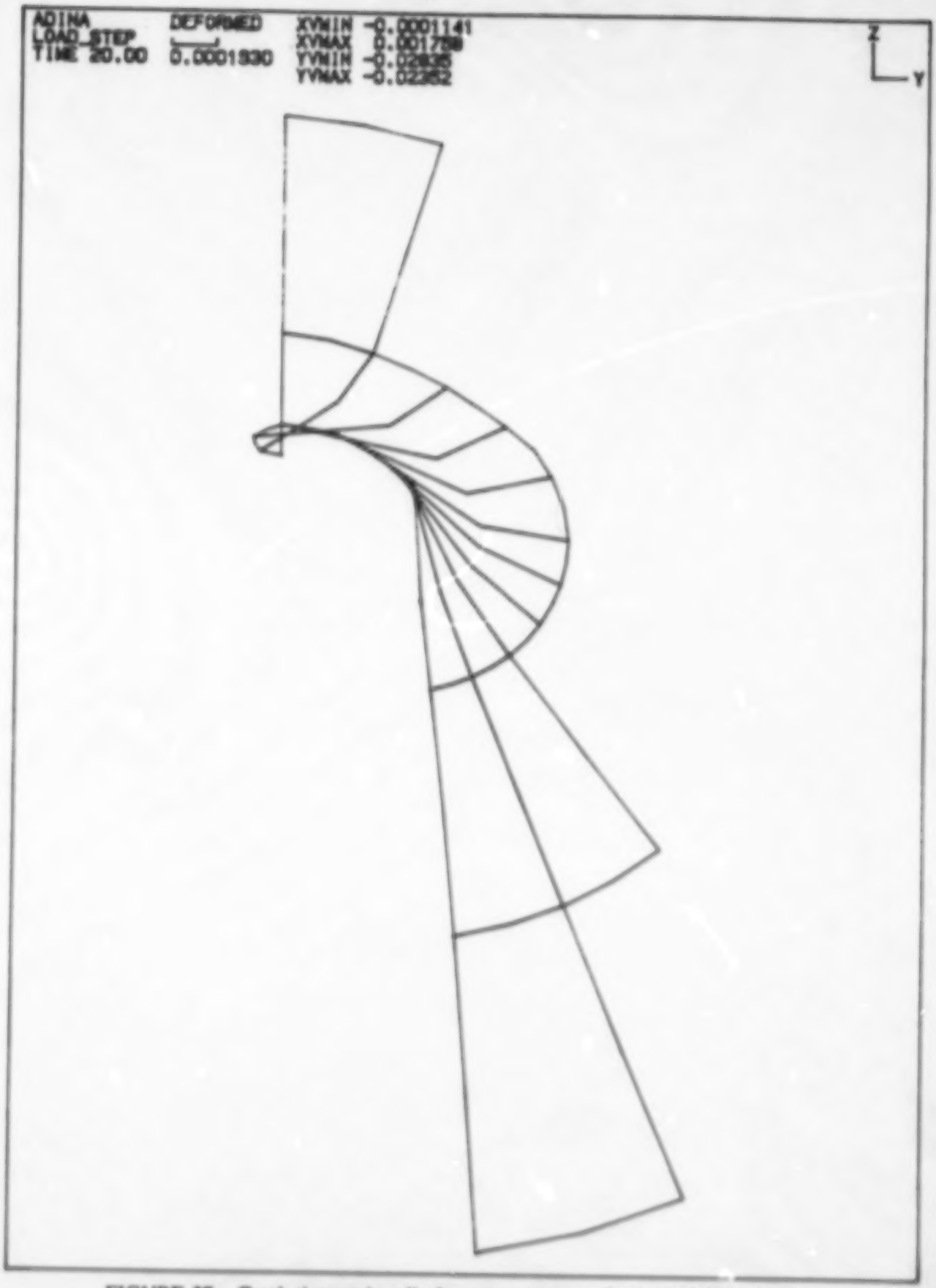

FIGURE 37. Crack tip opening displacement; pressure load of 13.375 MPa.

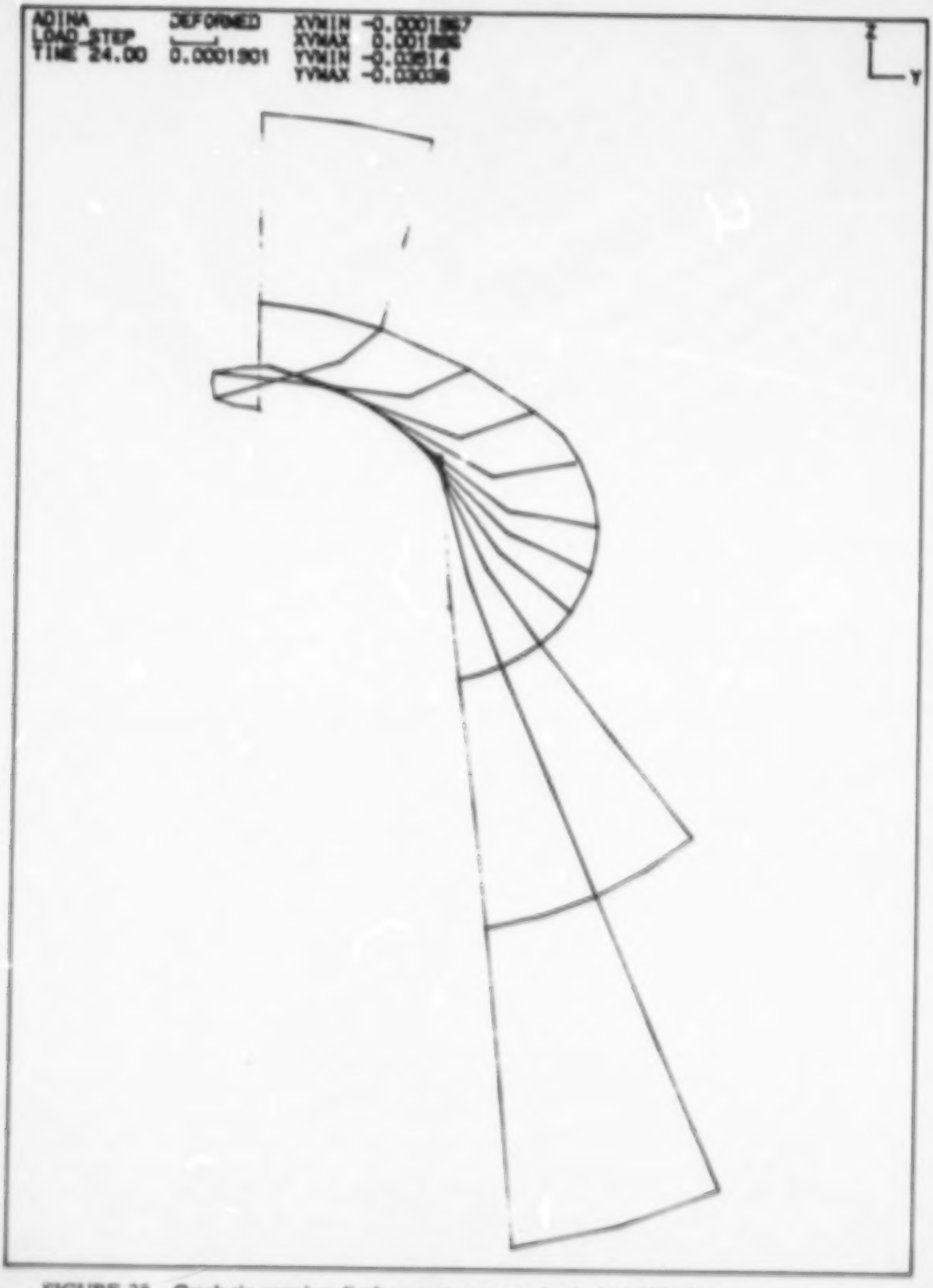

FIGURE 38. Crack tip opening displacement; pressure load of 14.725 MPa.

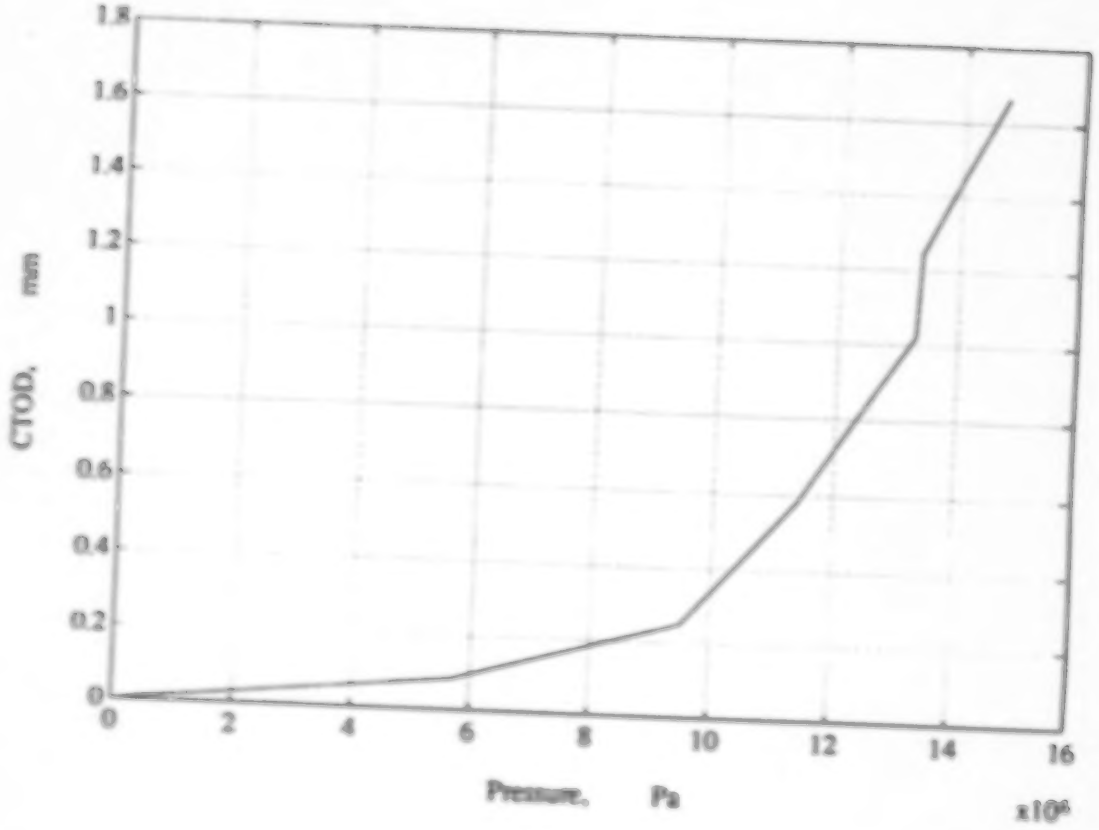

FIGURE 39. The effect of the pressure load on the crack tip opening displacement.

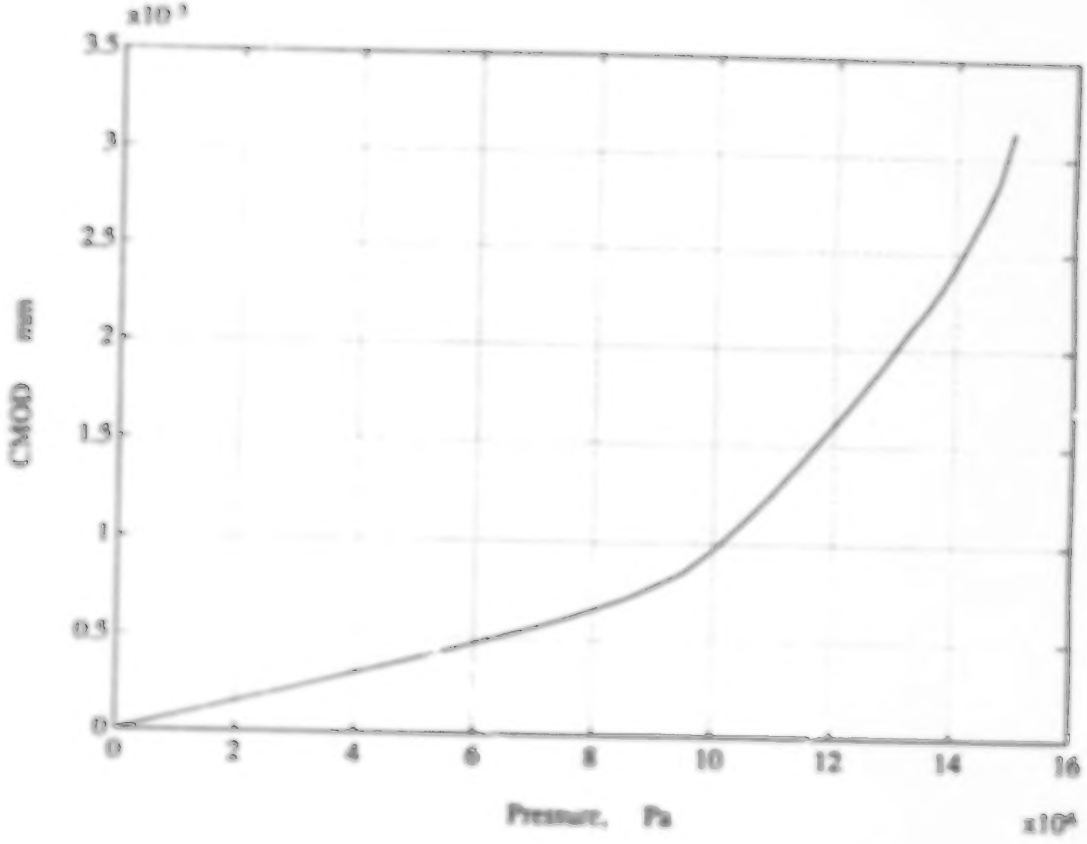

FIGURE 40. The effect of the pressure load on the crack mouth opening displacement.